Journal of Applied Meteorology and Climatology

A Hybrid Bulk Algorithm to Predict Turbulent Fluxes over Dry and Wet Bare Soils

--Manuscript Draft--

Manuscript Number:	JAMC-D-20-0232
Full Title:	A Hybrid Bulk Algorithm to Predict Turbulent Fluxes over Dry and Wet Bare Soils
Article Type:	Article
Corresponding Author:	Andrey Grachev, Ph.D. US Army Research Laboratory White Sands, NM UNITED STATES
Corresponding Author's Institution:	US Army Research Laboratory
First Author:	Andrey A. Grachev, Ph.D.
Order of Authors:	Andrey A. Grachev, Ph.D.
	Christopher W. Fairall
	Byron W. Blomquist
	Harindra J. S. Fernando
	Laura S. Leo
	Sebastián F. Otárola-Bustos
	James M. Wilczak
	Katherine L. McCaffrey
Manuscript Classifications:	4.040: Atmosphere-land interaction; 4.232: Fluxes; 4.264: Heat budgets/fluxes; 4.508: Water vapor; 8.160: Parameterization
Abstract:	Measurements made in the Columbia River Basin (Oregon) in an area of irregular terrain during the second Wind Forecast Improvement Project (WFIP 2) field campaign are used to develop an optimized hybrid bulk algorithm to predict the surface turbulent fluxes from readily measured or modelled quantities over dry and wet bare or lightly vegetated soil surfaces. The hybrid (synthetic) algorithm combines (i) an aerodynamic method for turbulent flow which is based on the transfer coefficients (drag coefficient and Stanton number), roughness lengths, and Monin-Obukhov similarity and (ii) a modified Priestley-Taylor (P-T) algorithm with physically based ecophysiological constraints which is essentially based on the surface energy budget (SEB) equation. Soil heat flux in the latter case was estimated from measurements of soil temperature and soil moisture. In the framework of the hybrid algorithm, bulk estimates of the momentum flux and the sensible heat flux are derived from a traditional aerodynamic approach, whereas the latent heat flux (or moisture flux) is evaluated from a modified P-T model. Direct measurements of the surface fluxes (turbulent and radiative) and other ancillary atmospheric/soil parameters made during WFIP 2 for different soil conditions (dry and wet) are used to optimize and tune the hybrid bulk algorithm. The bulk flux estimates are validated against the measured eddy-covariance fluxes. We also discuss the SEB closure over dry and wet surfaces at various timescales based on the modelled and measured fluxes. Although this bulk flux algorithm is optimized for the data collected during the WFIP 2, a hybrid approach can be used for similar flux-tower sites and field campaigns.

A Hybrid Bulk Algorithm to Predict Turbulent Fluxes over Dry and Wet Bare Soils

ANDREY A. GRACHEV [a, b, *], CHRISTOPHER W. FAIRALL [a], BYRON W. BLOMQUIST [a, b], HARINDRA J. S. FERNANDO [c], LAURA S. LEO [c, d], SEBASTIÁN F. OTÁROLA-BUSTOS [c], JAMES M. WILCZAK [a], KATHERINE L. MCCAFFREY [a, b, ♣]

[a] *NOAA Physical Sciences Laboratory, Boulder, CO, USA*
[b] *Cooperative Institute for Research in Environmental Sciences, University of Colorado, Boulder, CO, USA*
[c] *Department of Civil & Environmental Engineering & Earth Sciences, Department of Aerospace and Mechanical Engineering, University of Notre Dame, Notre Dame, IN, USA*
[d] *Department of Physics and Astronomy, Alma Mater Studiorum-University of Bologna, Bologna, Italy*

---

[*] Current affiliation: Boundary Layer Research Team/Atmospheric Dynamics & Analytics Branch, DEVCOM Army Research Laboratory, WSMR, NM, USA

[♣] Current affiliation: S & P Global Market Intelligence, Boulder, CO, USA

Corresponding author: Andrey A. Grachev, Andrey.Grachev@colorado.edu

---

Journal of Applied Meteorology and Climatology

Manuscript submitted: October 11, 2020
Revised: October 25, 2021

ABSTRACT

Measurements made in the Columbia River Basin (Oregon) in an area of irregular terrain during the second Wind Forecast Improvement Project (WFIP 2) field campaign are used to develop an optimized hybrid bulk algorithm to predict the surface turbulent fluxes from readily measured or modelled quantities over dry and wet bare or lightly vegetated soil surfaces. The hybrid (synthetic) algorithm combines (i) an aerodynamic method for turbulent flow which is based on the transfer coefficients (drag coefficient and Stanton number), roughness lengths, and Monin-Obukhov similarity and (ii) a modified Priestley-Taylor (P-T) algorithm with physically based ecophysiological constraints which is essentially based on the surface energy budget (SEB) equation. Soil heat flux in the latter case was estimated from measurements of soil temperature and soil moisture. In the framework of the hybrid algorithm, bulk estimates of the momentum flux and the sensible heat flux are derived from a traditional aerodynamic approach, whereas the latent heat flux (or moisture flux) is evaluated from a modified P-T model. Direct measurements of the surface fluxes (turbulent and radiative) and other ancillary atmospheric/soil parameters made during WFIP 2 for different soil conditions (dry and wet) are used to optimize and tune the hybrid bulk algorithm. The bulk flux estimates are validated against the measured eddy-covariance fluxes. We also discuss the SEB closure over dry and wet surfaces at various timescales based on the modelled and measured fluxes. Although this bulk flux algorithm is optimized for the data collected during the WFIP 2, a hybrid approach can be used for similar flux-tower sites and field campaigns.

1. Introduction

Determination of momentum, heat, and mass exchange between the atmosphere and the underlying surface is a central problem of atmospheric boundary-layer (ABL) research. Understanding and proper parameterization of the surface turbulent fluxes (e.g., flux-profile relationships) is of obvious relevance for the modelling of the coupled atmosphere-land/ocean system, including climate modelling, weather forecasting, environmental impact studies, and many other applications. It should be noted that with the exception of direct numerical simulations the surface fluxes are always subgrid- scale processes that cannot be explicitly resolved and must be parameterized, regardless of how high the resolution of a numerical model is. At present, in almost all numerical models, from local and mesoscale to global models (i.e., in weather prediction and climate models), turbulence fluxes are parametrized using Monin-Obukhov similarity theory (MOST) or/and a bulk flux algorithm.

A direct application of the turbulent energy fluxes is the net surface energy budget (SEB). An accurate determination of energy balance closure and all components of the SEB at the air-surface interface are required in a wide variety of applications including atmosphere-land/snow simulations and validation of the surface fluxes predicted by numerical models over representative spatial and temporal scales.

Recently, progress has been made in our understanding of the turbulent mixing and development of bulk schemes over, more or less, horizontally homogeneous surfaces such as the open ocean (e.g., the COARE bulk flux algorithm by Fairall et al. 1996, 2003) and snow covered sea ice (e.g., the SHEBA bulk turbulent flux algorithm by Andreas et al. 2010a, 2010b). Because of the complexity of vegetated and bare (or lightly vegetated) surfaces, an equivalent progress in development of simplified bulk algorithms over land is not as straightforward as in the case of the over water or snow/ice, but appears feasible in this case. In this study, surface fluxes (turbulent and radiative) and other ancillary atmospheric and soil data collected in the Columbia River Gorge area near Wasco, Oregon, during 2016-2017 within the second Wind Forecast Improvement Project (WFIP 2), are used to develop a hybrid bulk flux algorithm utilizing the available WFIP 2 experimental data.

The novelty of the present study is to develop a hybrid or synthetic (in the sense of "combination") bulk approach to predict the surface turbulent fluxes from tower-based measurements. Traditional bulk flux schemes (e.g., the COARE and SHEBA algorithms) derive all three turbulent fluxes (momentum, sensible, and latent heat) in the same way. The hybrid bulk flux algorithm developed in this study derives the turbulent fluxes of momentum and sensible heat from the traditional aerodynamic method for the turbulent flow (similar to the COARE and SHEBA algorithms), whereas the latent heat flux is estimated from a method which is essentially based on the conservation of energy principle (i.e., the surface energy balance at the surface–atmosphere interface). Although our bulk flux algorithm is based on the WFIP 2 data, the hybrid approach developed here can be applied to similar tower-based measurements over land to predict the turbulent fluxes.

The paper is organized as follows. The following section contains information about the observation site, instrumentation and dataset collection. Section 3 provides a formal background for measuring and modelling surface fluxes including the SEB closure problem and traditional bulk flux approach. In Section 4, we develop and verify a hybrid bulk flux algorithm for computing surface fluxes from readily measured or modelled during WFIP 2 bulk quantities. The conclusions are summarized in Section 5. Some material presented in the current study, e.g., associated with the description of the observation site, instrumentation, and data (Section 2), is partially repeated here from Grachev et al. (2020). Both studies use the same WFIP 2 dataset but for different problems.

2. Observation Site, Instrumentation, and Data

This study analyzes and discusses the data collected during a 10-month long portion of the second Wind Forecast Improvement Project (WFIP 2) field campaign (see Bianco et al. 2019; Olson et al. 2019; Shaw et al. 2019; Wilczak et al. 2019 for details). Grachev et al. (2020) described the measurement site, instruments, various observations, data processing etc. in detail. Here we provide some relevant information about the turbulent and profile measurements in the near-surface atmosphere and soil layer during the WFIP 2 project.

The WFIP 2 field campaign took place in an area of irregular terrain along the Columbia River Gorge in eastern Oregon and Washington states (Fig. 1). Here we use measurements of 30-min averaged surface fluxes and basic meteorological/soil parameters from the Physics Site 1 tower (PS01) located near Wasco (Oregon). The PS01 study area encompasses relatively flat plain (e.g. Fig. 2) and a ridge (e.g. Grachev et al. 2020, their Fig. 2) sited in irregular terrain of moderate complexity. The ridge is aligned approximately in a W–E direction. The instruments at the PS01 site (Figs. 1 and 2) were deployed in an area similar to a high-resolution model grid cell for observing subgrid-scale turbulent processes (Shaw et al. 2019). According to Grachev et al. (2020, their Fig. 3b), prevailing winds observed at PS01 site have a bimodal distribution with the two dominant wind directions ≈ 180° apart (easterly and westerly winds). These predominant winds generally blow parallel to the ridge and not frequent southerly wind directions are generally associated with lights winds. Turbulent fluxes and other ancillary atmospheric data at the PS01 site were measured continuously on a 10-m meteorological tower at 3 m and 10 m levels (Fig. 2) from 24 June 2016 to 01 May 2017, Year Days (YD) 176-487 with respect to January 1, 2016 UTC. Each level was instrumented with identical fast response three-axis sonic anemometers sampling wind velocity and sonic temperature at 20 Hz (R.M. Young Model 81000) and Rotronics HC2S3 temperature and relative humidity probes (T/RH, sampling frequency = 1 Hz). The HC2S3 probes were housed in ventilated radiation shields. A fast-response (20 Hz) infrared gas analyzer (LI-7500) was collocated at 3-m height with the lower sonic anemometer. The mean wind speed and wind direction were derived from the sonic anemometers using the ordinary planar-fit method rotation of the coordinate system proposed by Wilczak et al. (2001). Several data-quality indicators based on objective and subjective methods have been applied to the original flux data to remove spurious or low-quality records (e.g., Bariteau et al. 2010; Grachev et al. 2011, 2015; Blomquist et al. 2014 and references therein). Specifically, turbulent data have been edited for unfavorable relative wind direction for which the tower was upwind of the sonic anemometers, non-stationarity, minimum or/and maximum thresholds for the turbulent statistics, etc. In particular, sonic anemometer data based on the planar-fit procedure were flagged as bad if the mean vertical velocity component differed by more than 0.2 m s^{-1} from the plane. For example, after data-quality control screening, the number of data-points for sensible heat H_S and latent heat H_L fluxes measured at the level 3m during the entire WFIP 2 field campaign decreased to ≈ 90.2% and ≈ 79.6% of the original amount respectively.

Measurements of soil temperature and moisture were made at five levels located nominally at 5, 10, 20, 50, and 100 cm depths below the ground surface approximately 5 m from the flux tower. Note that no direct measurements of surface soil heat flux with a heat flux plate were performed at this site. The soils at the WFIP 2 Physics Site PS01 are primarily well-drained silt (73%), with minor components of sand (14%), and clay (13%) and average 152 cm in depth before reaching harder rock. In general, the underlying surface at the PS01 site can be described as bare and/or short vegetation surface (cf. Cuxart and Boone 2020, their Fig. 1). The downwelling and upwelling shortwave and infrared radiation was measured from two radiation masts located near the flux tower by Eppley pyranometers and pyrgeometers respectively (Fig. 2). The 'slow'-response data used in this study (T/RH, solar radiation, soil temperature and moisture) are based on 1 Hz raw measurements which were averaged over 1-min time intervals.

The time series of half-hour averaged surface fluxes and basic meteorological variables to describe weather and soil conditions, surface fluxes, and other relevant variables as observed during the entire WFIP 2 field campaign for the period 24 June 2016 to 01 May 2017 (YD 176-487 with respect to January 1, 2016 UTC) can be found in Grachev et al. (2020, Figs. 3-6). Similar to Grachev et al. (2020, Sect. 4.1), in this study we sort the data into dry and wet categories (the soil moisture content below is the volumetric soil moisture):

(i) **Dry bare (or lightly vegetated) soil surfaces**, if the soil temperature at 5 cm depth is > 1°C and the volumetric soil moisture at 5 cm depth is ≤ 0.07;

(ii) **Wet bare (or lightly vegetated) soil surfaces**, if the soil temperature at 5 cm depth is > 1°C and the volumetric soil moisture at 5 cm depth is > 0.07.

According to our data, dry and wet surfaces for this location and for the considered time intervals are generally associated with the volumetric soil moisture at 5 cm depth under 0.05 and above 0.15 respectively (Grachev et al. 2020, Fig. 4b). Range between 0.05 and 0.15 can be considered as a transition interval. However our data show that the surface soil moisture increases rapidly during approximately two days around YD 291 with the onset of the rainy season (Grachev et al. 2020, Fig. 4b-d). Thus, transition from the dry-soil case to the wet-soil case has occurred within a fairly short period of time and, for this reason, the choice of any value from the transition range as a threshold (e.g., 0.07) has little or no effect on the final results.

The original 10-month long in situ data often contain gaps (Grachev et al. 2020, Figs. 3-6). To calibrate and verify the bulk flux algorithm over different soil conditions, we use in this study a 30-day long uninterrupted time series of relatively good data separately for dry and wet soil conditions (WFIP 2 "golden files") described by Grachev et al. (2020, Sect. 4.4). Data collected during year days 240–270 (27 August-26 September 2016) provide an illustrative example of surface meteorology and surface fluxes observed at the WFIP 2 Physics site PS01 for dry soils. Similarly the 30-day long time period from 25 March to 24 April 2017 (YD 450–480 with respect to 1 January 2016) was selected to analyze data over wet soil surfaces.

Figures 3-6 show continuous monthly (30-day long) records of the surface fluxes and surface meteorology for dry and wet soils respectively. The data presented in Figs. 3-6 and some other ancillary information for these time periods are used in this study to test the bulk algorithm. Additionally, the time-series of the SEB components (the net radiation, the sum of the sensible and latent heat fluxes, the SEB residual) over dry and wet soils for the same time periods as in Figs. 3-6 in the current study can be found in Grachev et al. (2020, Figs. 10 and 11). Thereby, we use a subset of the data analyzed in our previous study (Grachev et al. 2020), though of a higher quality.

As expected, variations of the air temperature, topsoil temperature, and the turbulent energy fluxes, H_S and H_L, have a pronounced diurnal cycle (Figs. 3-6). We note different behavior of H_S and H_L for different soil conditions. According to Fig. 4a and Fig. 6a, values of the half-hourly H_S at local noon are generally larger for drier than for wetter soils, whereas the situation with H_L is obviously opposite. The turbulent flux of the latent heat shown in Fig. 4b is small over dry soil surfaces indicating that evaporation is negligible for drier than for wetter soils (cf. Fig. 6b). Furthermore, diurnal variations of H_L are much less evident in the case of dry soil conditions (Fig. 4b). Note also that in general the soil moisture increases with increasing depth for dry soils (Fig. 3d) and vice versa for wet soils (Fig. 5d).

Other details regarding the observation site, the instrumentation, and the data can be found in Grachev et al. (2020).

3. Measuring and Modeling Surface Fluxes

The turbulent fluxes of momentum τ (or magnitude of the wind stress), sensible heat H_S, and latent heat H_L can be estimated by the eddy-correlation method according to

$$\tau = \rho u_*^2 \tag{1}$$

$$H_S = c_p \rho \overline{w'\theta'} = -c_p \rho u_* \theta_* \tag{2}$$

$$H_L = \mathcal{L}_e \rho \overline{w'q'} = -\mathcal{L}_e \rho u_* q_* \tag{3}$$

where ρ is the mean air density, θ is the air potential temperature, q is the air specific humidity, c_p is the specific heat capacity of air at constant pressure, $\mathcal{L}_e$ is the latent heat of evaporation of water, $u_*^2 = \sqrt{(\overline{w'u'})^2 + (\overline{w'v'})^2}$ (u_* is the friction velocity), $\theta_* = -\overline{w'\theta'}/u_*$ and $q_* = -\overline{w'q'}/u_*$ are the temperature and the specific humidity scales respectively. Here w is the vertical velocity component, the prime [$'$] denotes fluctuations about the mean value, and an overbar is an averaging operator (half an hour in this study). Note that in Eq. (1), τ is based on the both longitudinal (or downstream), $\tau_x = -\rho\overline{w'u'}$, and the lateral (or crosswind), $\tau_y = -\rho\overline{w'v'}$, components of wind stress (see Grachev et al. 2011 for discussion).

a. SEB Closure

Knowledge of the surface energy fluxes (2) and (3) is considered fundamental to the surface energy budget (SEB). Typically, the SEB equation accounts for energy inputs and outputs at the infinitesimal interface between atmosphere and land and it is assumed that the energy budget must balance; that is, the SEB equation is a balance equation. Thus, the classical formulation of the SEB equation is:

$$H_S + H_L + G = R_{net} \tag{4}$$

where G is the soil heat flux, R_{net} is the net radiation defined as the balance between downwelling and upwelling SW and LW radiation:

$$R_{net} = SW_{down} - SW_{up} + LW_{down} - LW_{up} \tag{5}$$

Note that unlike the momentum flux τ (1), the turbulent energy fluxes H_S and H_L are highly correlated with the net radiation R_{net} due to the SEB equation (e.g., Grachev et al. 2020, Fig. 8), providing an objective approach for a land-surface model or numerical models of the climate system to estimate missing terms (e.g., H_S or H_L) as the residual of the others based on (4) which is traditionally considered to have to be closed (e.g., Cuxart et al. 2015 and references therein). A similar approach is used in soil-vegetation-atmosphere transfer schemes where the surface energy fluxes are estimated from thermal infra-red data (i.e. radiometric surface temperature) and SEB, Eq. (4) (e.g., Priestley and Taylor 1972; Su 2002; Kustas et al. 1993, 2004; Yao et al. 2015 and references therein). In the next section, we develop a method of estimating H_L on the basis of the surface energy balance.

In practice, the soil heat flux G in (4) can be measured at some reference depth z below the ground surface by a heat flux plate or estimated from soil temperature profile measurements using Fourier's Law of Heat Conduction (gradient method):

$$G(z) = -\lambda \frac{\partial T_S}{\partial z} \tag{6}$$

where λ is the thermal conductivity of the soil and $\partial T_S/\partial z$ is the vertical temperature gradient of the soil temperature, T_S. Traditionally, $\partial T_S/\partial z$ in the soil layer Δz is replaced by $\Delta T_S/\Delta z$ and Eq. (6) reduces to $G(z) \approx -\lambda \Delta T_S/\Delta z$.

Surface energy balance closure (4) is a formulation of the conservation of energy principle at the interface and Eq. (4) assumes an ideal case, when all the fluxes are measured at the infinitesimal interface between the atmosphere and the soil and it is a statement of how the net radiation (5) is balanced by turbulent sensible (2), latent (3), and soil (6) heat fluxes in the absence of other energy sources and sinks. However, many studies reported that the surface energy balance (4) is difficult to close at temporal scales less than several hours (e.g., Wilson et al. 2002; Foken et al. 2006; Mauder et al. 2007, 2020; Cava et al. 2008; Foken 2008; Jacobs et al. 2008; Higgins 2012; Leuning et al. 2012; Stoy et al. 2013; Cuxart et al. 2015; Majozi et al. 2017; Gao et al. 2017a; Grachev et al. 2020 and references therein). Direct measurements of energy budget at these time scales (in particular, at half-hourly and hourly averaged time scales) showed that in most cases the sum of the turbulent fluxes of sensible and latent heat plus the ground heat flux systematically is lower than the net radiation by around 20-30% during daytime and generally is higher than the net radiation at night.

Because the fluxes cannot be measured at the surface and the energy balance often cannot be closed based on experimental data, the SEB equation (4) is re-formulated for a control volume instead of at the interface of the two media (e.g., Foken et al. 2006; Mauder et al. 2020):

$$H_S + H_L + G + Res = R_{net} \tag{7}$$

where Res is a residual term. Note, that Eq. (7) implies now a two-layer (atmosphere and soil) column of finite thickness (e.g., Foken 2008, his Fig. 1) where the turbulent fluxes (1)-(3) and the net radiation (5) are measured at the upper boundary plane whereas the soil flux is measured at the lower boundary plane of the total layer respectively. In the general case, Res can be partitioned as the sum of an additional transport (vertical and horizontal) term through all boundary planes, a total storage term in the two-layer column (air and soil), and all other reasons unaccounted in (4) which can be also responsible for the SEB imbalance. The storage term in turn can be partitioned as a sum of storage of energy in the air column due to radiative and/or sensible heat flux divergence (the air enthalpy change), ground heat storage above a near-surface reference point, radiation consumed in photosynthesis (the photosynthesis flux), canopy heat storage in biomass (the rate change in enthalpy of the vegetation), as well as all other storage terms (e.g., Meyers and Hollinger 2004, Jacobs et al. 2008; Leuning et al. 2012, Masseroni et al. 2014).

A variety of factors (except of H_S, H_L, R_{net}, and G) may be responsible for the lack of SEB closure. For example, failure to close the energy balance may be associated with storage of energy in the air column due to radiative and/or sensible heat flux divergence (the air enthalpy change), the ground heat storage above a heat flux plate measurement level, the radiation consumed in photosynthesis (the photosynthesis flux), the canopy heat storage in biomass (the rate change in enthalpy of the vegetation), and other storage terms, e.g. the atmospheric moisture change and the canopy dew water enthalpy change (e.g., Mauder et al. 2020). In addition, another complexity of the SEB closure is associated with non-stationarity (diurnal variations), even during a half-hour averaging period (e.g., Garratt 1992). The diurnal cycle of solar radiation modulates a sinusoidal variation in the ground surface heat flux and diurnal thermal waves in the top soil layer. The impact of the hysteresis effect in diurnal cycles and the effect of the wave phase difference between different atmospheric and/or soil variables on the SEB closure are discussed in number of studies (e.g., Gao et al. 2017a and references therein). It is generally accepted that the underestimation of the sensible and latent heat fluxes is associated with large-scale non-turbulent transport mechanisms at low-frequencies such as boundary-layer scale eddies under convective conditions, mesoscale and sub-mesoscale transport, secondary circulations etc. (Foken 2008; Mauder et al. 2020). According to Grachev et al. (2020), extending the averaging time consistently from half-hourly to daily, weekly, monthly, seasonal, and sub-annual timescales (311-day averaging for the entire WFIP 2 field campaign) significantly reduces the SEB imbalance on average. Increasing the averaging time to daily and longer time intervals substantially reduces averaged ground heat flux and storage terms, because energy locally entering the soil, air column, and vegetation in the morning and during the first half of the day is released in the afternoon, evening, and night.

b. Traditional Bulk Turbulent Flux Algorithm

In almost all numerical weather prediction and climate models the turbulent fluxes of momentum τ, sensible heat H_S, and latent heat H_L, Eqs. (1)-(3), are estimated using MOST or/and a bulk flux algorithm. In this study, we will use a bulk formulation, which is in part based on the COARE bulk flux algorithm derived for open ocean (Fairall et al. 1996, 2003), and the SHEBA bulk flux algorithm developed for sea ice conditions (Andreas et al. 2010a, 2010b). We will use observations from the WFIP 2 Physics Site PS01 to evaluate bulk representations of the turbulent and ground fluxes, including the turbulent surface stress, τ, because u_* is required for surface layer similarity theory that forms the basis of bulk turbulent flux algorithms.

The turbulent fluxes are parameterized by bulk aerodynamic relationships, which relate fluxes to mean properties of the flow through the height-dependent transfer coefficients: C_D (the drag coefficient), C_H (the Stanton number), and C_E (the Dalton number):

$$\tau = C_D \rho S U \, , \tag{8}$$

$$H_S = C_H c_p \rho S \Delta\theta \, , \tag{9}$$

$$H_L = C_E \mathcal{L}_e \rho S \Delta q \, , \tag{10}$$

Here $\Delta\theta = (\theta_0 - \theta_a)$ and $\Delta q = (q_0 - q_a)$, where subscripts 'zero' and a for the potential temperature θ and the air specific humidity q denote their surface ('skin', $z = 0$) and atmospheric reference height values respectively. It is often assumed that the water vapor and other scalars (e.g. carbon dioxide and methane) are transported similarly to the temperature, i.e. with the same efficiency (the Lewis analogy) and, therefore, $C_H = C_E$. Note, that accurate estimation of the transfer coefficients in (8)–(10) is a crucial problem of air-sea/land interaction. The transfer coefficients depend on stratification (atmospheric stability) and roughness lengths (e.g., Fairall et al. 1996, 2003). Scalar averaged wind speed S in (8)–(10) is defined and discussed in the Appendix.

4. Hybrid Bulk Algorithm and Analysis of the WFIP 2 Data

Following the discussion in the Section 3 and in the Appendix, turbulent fluxes are computed from (8) – (10) and ($A4$) via an iteration because the transfer coefficients depend on the MOST stability parameter z/L which is computed from the fluxes (see Fairall et al. 1996, 2003). The forms of (8)–(10) apply well to reasonably statistically homogeneous surfaces where an interfacial value of q_0 can be unambiguously established - oceans, lakes, ice, snow covered surfaces, or water-saturated soils where we can assume q_0 is the water saturation value at temperature θ_0. For dry and wet bare soils or simple ground-hugging plant canopies, Eq. (8) and (9) still work but in general case (10) does not apply because the surface is not near saturation. Kondo et al (1990) show that application of Eq. (10) for parameterization of evaporation from bare soil surfaces requires coupling with a special model of molecular diffusion of water vapor in the surface soil pore with the vapor being carried from the interior of the soil pore to the land surface.

Various techniques to represent H_L over land surfaces have been reported in the literature (see Garratt 1992; Foken 2017 for background). The most widely used model is the physically-based Penman-Monteith (hereinafter P-M) model (Penman 1948; Monteith 1965; De Bruin and Holtslag 1982) which combines the SEB and aerodynamic transport equations, assuming that surface meteorological observations are available. An alternative approach, the Priestley-Taylor (hereinafter P-T) algorithm is relatively simple, and can be considered as a simplified P-M method that avoids parameterizations of aerodynamic and surface resistance without decreasing the accuracy of the H_L estimates (Priestley and Taylor 1972). Both the P-M and P-T methods have been shown to give relatively low biases, particularly in comparison with the relatively poor accuracy of other methods (Fisher et al. 2008).

The SEB equation (4), which is assumed to be closed, is the starting point in the P-T model. The Bowen-ratio method and the Clausius-Clapeyron equation are also used in the derivation of the P-T relationship (e.g., Foken 2017). Although the original P-T method (Priestley and Taylor 1972) was developed for saturated surfaces, it has been widely extended to unsaturated surfaces. Different modified P-T models are based on parameters that relate the saturated and unsaturated surfaces and parameterization of the atmospheric and resistance variables ("constraint functions"). Further discussion regarding various modifications of the P-T model can be found in De Bruin (1983), Fisher et al. (2008), Venturini et al. (2011), Yao et al. (2013, 2014, 2015), and Hao et al. (2019) among others. The P-T model stands for its simplicity and low data requirements (e.g., where ground observations of aerodynamic and surface resistance is not available) and for this reason the P-T approach is widely used as a satellite-based H_L-algorithm and remote sensing technology that enables estimation of the terrestrial H_L at regional or global scales (e.g., Fisher et al. 2008; Li et al. 2009; Venturini et al. 2011; Yao et al. 2013, 2014, 2015). Further discussion, the state of the art, and perspectives on determining evapotranspiration by various methods (including MOST, P-M and P-T approaches) can be found in a review paper by Cuxart and Boone (2020).

In this study, we follow a modified P-T model by Yao et al. (2015) to estimate H_L over dry and wet bare soils during the WFIP 2 field campaign. The approach by Yao et al. (2015) combines the P-T method which avoids the uncertainty associated with the Dalton transfer coefficient and an effective surface relative humidity in (10) with physically based ecophysiological constraints. According to a modified P-T model by Yao et al. (2015), the latent heat flux H_L can be expressed as:

$$H_L = \alpha \frac{\Delta_s}{\Delta_s + \gamma} f(e)(R_{net} - G) \qquad (11)$$

where Δ_s is the temperature derivative from the saturated vapor pressure relationship (see Priestley and Taylor 1972 for detail), γ the psychrometric constant, $f(e)$ the sum of the weighted ecophysiological constraints, and α the P-T parameter. According to Priestley and Taylor (1972), the empirical parameter α in (11) equal to 1.26 on average for saturated surfaces. In general, the P-T parameter α varies with soil moisture, the canopy resistance, thermal stratification, etc. and has a diurnal cycle (e.g., De Bruin 1983; Lhomme 1997; Pereira 2004; Cristea et al. 2013; Assouline et al. 2016; Cuxart and Boone 2020). In particular, the P-T parameter α increases as the surface resistance to the evapotranspiration decreases; i.e., α increases with increasing the soil moisture (Cristea et al. 2013) and, according to De Bruin (1983), $\alpha > 1$ for well-watered surfaces and $\alpha < 1$ under dry conditions.

The value of $f(e)$ in (11) varies from 0 to 1. According to Yao et al. (2015, Eq. 11), the ecophysiological constraint function $f(e)$ in (11) can be expressed as

$$f(e) = k_0 + k_1\theta_a + k_2RH^{VPD} + (k_3NDVI - k_4)VPD \quad (12)$$

where VPD is the air vapor pressure deficit $e_{sat}(\theta) - e$, RH the relative humidity (0 to 1), and $NDVI$ the normalized difference vegetation index. The k_i (i = 0, …, 4) are empirical coefficients given in Table 1 of Yao et al. (2015) for nine different surface types. We have chosen a type 'GRA' (Yao et al. 2015, their Table 1), which includes grassland and barren or sparsely vegetated soil (soil at the PS01 tower site is essentially a plowed fallow field with little vegetation).

In order to calculate H_L from a P-T type model, the soil heat flux G in (11) needs to be estimated. As mentioned earlier, we do not have direct measurements of the soil heat flux G at the WFIP 2 Physics Site PS01. There are numerous approaches to compute the soil heat flux, that use different input data from in situ measurements (e.g., see Liebethal et al. 2005; Liebethal and Foken 2007; Gao et al. 2017b). Different methods for evaluating G can use various in situ measurements such as soil temperature, soil moisture, net radiation, etc. Furthermore, some parameterization approaches can be suitable for different times of the day. Here, we use measurements of soil temperature, $T_S(z)$, and soil moisture, $Q_S(z)$, to estimate G in (11) based on (6). Eq. (6) can be now integrated for the interface down to some reference depth Δz. Near the surface we can linearly approximate $G(z)$, so

$$\int_0^{\Delta z} \left(G + z\frac{\partial G}{\partial z}\right) dz = G\Delta z + \frac{1}{2}\frac{\partial G}{\partial z}\Delta z^2 = \lambda[\theta_0 - T_S(\Delta z)] \tag{13}$$

In this notation G in (13) is the value at the interface $z = 0$ where also $T_S(0) = \theta_0$ (cf. Eq. 8). The gradient term in (13) is estimated from the temporal change of the soil temperature

$$\rho_S c_{pS} \frac{\partial T_S}{\partial t} = -\frac{\partial G}{\partial z} \tag{14}$$

where ρ_S is the soil density and c_{pS} is the soil specific heat. Thus, G can be estimated as the sum of a gradient and storage term (Garratt 1992)

$$G = \frac{\lambda}{\Delta z}[\theta_0 - T_S(\Delta z)] + \frac{1}{2}\rho_S c_{pS} \frac{\partial T_S}{\partial t} \Delta z \tag{15}$$

The system of the hybrid bulk flux computations is summarized in Table 1. Execution of these requires specification of certain coefficients which we have determined by tuning to agree with direct measurements at the PS01 site. Some other properties, such as Δ_s and γ in Eq. (11), or atmospheric stability functions, are considered universal and we take them from the literature. For the turbulent fluxes, we need to determine the transfer coefficients C_H and C_D. Following the discussion in the Appendix, we can estimate the 10-m neutral coefficients directly via

$$C_{X10n} = \frac{\overline{w'x'}}{U_{10n}\Delta X_{10n} G_f} \tag{16}$$

where $x = u$, θ, or q, $X = U$, θ, or q, and $\Delta X = X_0 - X_a$ is the difference between the surface value (zero for wind speed U) and the value at reference height z in the atmosphere, G_f is the gustiness factor (see the Appendix). Application of (16) is problematic when U_{10n} and/or ΔX_{10n} are small. We can set minimum thresholds U_{th} and ΔX_{th} for U_{10n} and ΔX_{10n} respectively and average (16) for a subset of the data restricted to conditions where $U_{10n} > U_{th}$ and $|\Delta X_{10n}| > \Delta X_{th}$. A variation on this approach is to do a linear regression of the form

$$\frac{\overline{w'x'}}{U_{10n}G_f} = a_x + b_x \Delta X_{10n} \quad (17)$$

so that $C_{X10n} = b_x$. This has advantages for the heat flux because we do not have to restrict $\Delta\theta_{10n}$ and the offset coefficient a_x in (17) gives an indication of relative bias between θ_0 and θ_a. If there is no bias, the regression should pass through the origin; a temperature bias would be indicated as $\delta X = -\, a_x/b_x$. An example of half-hourly averaged covariance sensible heat flux normalized by $c_p \rho U_{10n} G_f$ versus 10-m neutral surface-air temperature difference for the uninterrupted 30-day time series ("golden files" periods) is shown in Fig. 7 separately for dry soils (upper panel) and for wet soils (lower panel). In this case we examined fits where we have ignored observations with low wind speed (thresholds of U_{th} = 1 ms^{-1} and 4 ms^{-1} are used). These thresholds were selected based on a visual analysis of the data scatter in Fig. 7 and similar plots. The obvious outliers occur for winds less than 4 ms^{-1} but the fits yield about the same value for the Stanton number C_{H10n}, about $2.20 \cdot 10^{-3}$ using (16) and $2.15 \cdot 10^{-3}$ using (17) for dry soils (the uninterrupted 30-day time series, YD 240–270, 27 August-26 September 2016; see Fig. 3 and Fig. 4). For wet soils (the uninterrupted 30-day time series, YD 450–480, 27 25 March-24 April 2017; see Fig. 5 and Fig. 6), the corresponding values of C_{H10n} are $2.30 \cdot 10^{-3}$ using (16) and $2.39 \cdot 10^{-3}$ using (17). Similarly, results for the drag coefficient C_{D10n} are $2.76 \cdot 10^{-3}$ (16) and $2.29 \cdot 10^{-3}$ (17) for dry soil "golden files" (YD 240–270) and $3.63 \cdot 10^{-3}$(16) and $3.21 \cdot 10^{-3}$ (17) for wet soil "golden files" (YD 450–480) for the thresholds of U_{th} = 1 ms^{-1} and

4 ms^{-1} (plots for C_{D10n} similar to Fig. 7 are not shown here). Note that the number of data-points for the sensible heat measured during the dry soil "golden files" period (Fig. 7a) decreased to ≈ 97% of the original amount for wind speed greater than 1 ms^{-1} and ≈ 59% of the original amount for wind speed greater than 4 ms^{-1} respectively. Similar values for the wet soil "golden files" period (Fig. 7b) were ≈ 94% and ≈ 48% respectively.

A similar approach can be used to determine the ground flux; for Eq. (15) we do a linear regression of the form

$$G_{res} - \frac{1}{2}\rho_S c_{pS} \frac{\partial T_S}{\partial t} \Delta z = a_g + b_g[\theta_0 - T_S(\Delta z)] \quad (18)$$

so that $\lambda/\Delta z = b_g$. Because we do not have direct measurements of G, we have substituted the residual from an assumed energy balance

$$G_{res} = R_{net} - H_S - H_L \quad (19)$$

Thus, the residual term Res (all storage and transport contributions as well as other unspecified processes) in Eq. (7) is attributed in our model to the ground heat flux, i.e., by $G_{res} = G + Res$. Based on this assumption, we apply a linear fit in Eq. (18) to calibrated the model. Note that Mauder et al. (2020, Section 4) recently surveyed different methods when Res is attributed to H_S or H_L in order to to close energy balance.

An example for the dry soil "golden files" period (YD 240–270) and the wet soil "golden files" period (YD 450–480) is shown in Fig. 8. Here we have plotted the individual half-hourly values (Fig. 8) and, to reduce the noise, values from the mean diurnal cycle (Fig. 9). The fit yields a value of $\lambda/\Delta z$ = 2.859 $\mathrm{Wm}^{-2}\mathrm{K}^{-1}$ and 7.034 $\mathrm{Wm}^{-2}\mathrm{K}^{-1}$ for dry and wet soils respectively. We have done these fits for 15-day increments throughout the entire experimental period (311-day dataset from 24 June 2016 to 01 May 2017, YD 176–487) and found that the thermal conductivity of the soil, λ, varies considerably but with a strong correlation to soil moisture (see discussion in Appendix 4 of Garratt 1992). This correlation is illustrated in Fig. 10. Thus, based on the data presented in Fig. 10 for the entire field campaign, we estimate λ via

$$\lambda = 0.180 + 1.09Q_{S5} \tag{20}$$

where Q_{S5} is the soil moisture measured at 5 cm depth. Of course, by tuning the coefficients to the residual flux, we are forcing our parameterization to, on average, produce a reasonable total energy balance.

We also examined the use of (11) and (12) to estimate the latent heat flux H_L. We chose coefficients appropriate for bare soil from Yao et al (2015). However, we found that a constant value for the P-T coefficient α gave poor results. So we adjusted α in (11) to give a reasonable estimate of the mean flux and, as with the soil conductivity, we fit the values to soil moisture:

$$\alpha = 0.4 + 5Q_{S5} \tag{21}$$

This is in good agreement with the values reported in literature for dry and well-watered surfaces (e.g., De Bruin 1983; Cristea et al. 2013; Assouline et al. 2016). Note, however, that Eq. (21) for the P-T parameter derived from the WFIP 2 data is not a universal formula.

An example comparing direct covariance and bulk estimates of the sensible and latent heat fluxes for the dry and wet soil "golden files" is shown in Fig. 11. According to our half-hourly averaged data for the sensible heat flux H_S, the linear regression forced through the origin is $y = 1.02x$ with the correlation coefficient $R^2 = 0.99$ in the case of the dry soil "golden files" (Fig. 11a) and the regression is $y = 0.97x$ with $R^2 = 0.98$ in the case of the wet soil "golden files" (Fig. 11b) respectively. Thus, on average, the scatter plots for H_S (Fig. 11a and Fig. 11b) show a fairly good agreement between direct covariance and bulk estimates. The scatter in the sensible heat flux is about what we expect for covariance sampling error over half-hour averages (at least possible biases associated with the bulk flux algorithm are within the accuracy of the field turbulence data of ≈ 20-30%, see Yaglom, 1974). The scatter and bias between bulk and direct half-hour values of latent heat flux for the dry period (Fig. 11c) is considerably greater than that obtained for sensible heat flux but comparable to that for H_S for the wet period (Fig. 11d). According to our data, the linear regression forced through the origin is $y = 0.57x$ with the correlation coefficient $R^2 = 0.56$ in the case of the dry soil "golden files" (Fig. 11c) and the regression is $y = 0.93x$ with $R^2 = 0.88$ in the case of the wet soil "golden files" (Fig. 11d) respectively. The scatter plots of the measured turbulent fluxes versus their bulk counterparts (Fig. 11) can be considered as a validation test for our hybrid bulk flux algorithm.

One further point to consider is the nature of tuning coefficients in the context of imperfect observations. If we examine (9) we see one primary coefficient C_{H10n} and three observational variables S, θ_0, and θ_a. In principle, we could tune the transfer coefficient to give the correct observed mean flux for some period. Alternatively, we could look for inconsistencies in the observables and perhaps apply a correction. It is clear that θ_0 is subject to significant error, on the order of 1°C, because it is computed from upward and downward radiative fluxes which are each uncertain by roughly 5 Wm^{-2} (e.g., see specifications for Eppley PIR pyrgeometer). Also, note that both G and LW_{up} contain θ_0, so adjusting θ_0 will affect their mean values. Another factor is that for time periods of a few weeks, the variance of each of the fluxes is dominated by the diurnal cycle. A summary of flux statistics (monthly mean and standard deviation) for the dry and wet soil "golden files" periods is given in Tables 2 and 3 respectively. Values in Tables 2 and 3 are based on the data presented in Fig. 11. So, if we take the mean diurnal cycle of one of the fluxes (e.g., Fig. 9), we can diagnose the relevant errors in transfer coefficients or conductivity versus biases in the observed temperatures. The strength of the diurnal cycle is principally proportional to C_{H10n} or λ. If the difference in the day-night excursions of the bulk fluxes matches the observed fluxes, then the coefficients are about right. Offsets in the mean diurnal cycles can be reduced by 'correcting' θ_0, T_S, or θ_a. For sensible heat the slope from (17) yields the transfer coefficient that will match the diurnal cycle and the intercept indicates if there is a mismatch between θ_0 and θ_a. The small intercept bias in Fig. 7 gives an indication of relatively good correlation between the sensible heat flux H_S and $\Delta\theta_{10n}$ under the assumption that θ_0 and θ_a were accurately measured. Both Figs. 7 and 8 indicate reasonable compatibility of θ_0 and T_{S5}. Although in general, the bulk flux estimates provide reasonable renditions of the mean and standard deviation of the fluxes and the mean diurnal cycles (Fig. 12), the bulk estimates of the latent heat flux are somewhat higher than the measured ones during the daytime for dry soils (Fig. 12a). The sum of the three bulk fluxes yields a reasonable balance of the net radiation at half-hour time scales (Fig. 13). According to Fig. 13, the linear regression forced through the origin for the half-hourly data is $y = 1.10x$ for the dry soil "golden files" and $y = 0.98x$ for the wet soil "golden files".

As mentioned earlier, direct measurements of the soil heat flux G with a heat flux plate were not available during the field campaign WFIP 2. However, we use model estimates of G from the bulk flux algorithm described in this section to make estimates of the SEB closure (4). Figure 14 shows the net surface energy balance based on the measured sensible and latent heat fluxes $H_S + H_L$ and bulk estimates of the ground heat flux G_b versus the net solar radiation R_{net}. Two upper panels (*a*, *b*) show incomplete energy balance equation, $H_S + H_L$ vs. R_{net}, whereas two lower panels (*c*, *d*) are based on Eq. (4), $H_S + H_L + G_b$ vs. R_{net}. Plots in the left panels (*a*, *c*) represent the dry soil "golden files" (YD 240–270, 27 August-26 September 2016) and the right panels (*b*, *d*) represent the wet soil "golden files" period (YD 450–480, 25 March-24 April 2017).

According to the data presented in Fig. 14, the SEB imbalance in the case of the incomplete energy balance equation, that is; $H_S + H_L$ vs. R_{net}, is about 20% for dry soils (Fig. 14a), and is about 27% for wet soils (Fig. 14b) for half-hourly averaged fluxes. However, including the bulk estimates of the ground heat flux G_b in the SEB closure equation, that is; $H_S + H_L + G_b$ vs. R_{net}, substantially reduces the SEB imbalance for each specific soil condition, (to about 5%, Fig. 14c, and 3%, Fig. 14d, respectively). The SEB imbalance is also reduced for 30-day averaged data (cf. Figs. 14a, 14b and Figs. 14c, 14d respectively). Note that plots of monthly means in Grachev et al. (2020, Fig. 13) (triangular symbols for dry and wet soils) and in Fig. 14 (blue and pink six-pointed star symbols) are based on the data presented in Tables 2 and 3.

Although the entire 311-day experimental period (YD 176–487) is used for regression fit of the soil thermal conductivity soil in Fig. 10, the model is calibrated based on the data collected during two 30-day "golden files" time periods separately for dry (YD 240–270) and wet (YD 450–480) soils (Figs. 3-6). In the same time, the "golden files" periods are used for model verification (Fig. 11-14) what may not look quite correct. Therefore, for the independent model verification we tested our model beyond the calibration periods (the "golden files" periods). We have selected two additional 15-day test periods for dry (YD 270–285) and wet (YD 435–450) soil conditions and then apply the model without further tuning. The choice of is these time intervals associated with the availability of uninterrupted time series of relatively good data (see Grashev et al. 2020, Figs. 4–6). The results are shown in Figs. 15 and 16 and, as expected, they did not change significantly as compared to the calibration "golden files" periods (cf. linear regressions and correlation coefficients for pairs Fig. 15 – Fig. 11 and Fig. 16 – Fig. 13).

5. Summary and Discussion

While progress has been made in studying and in parameterizations turbulent fluxes of momentum, heat, and water vapor over horizontally homogeneous surfaces such as open ocean (Fairall et al. 1996, 2003) and sea ice or snow covered surfaces (e.g., Andreas et al. 2010a, 2010b), an equivalent level of progress in the development of simple bulk algorithms over land is not practical because of the complexity of the surface. Here we examine a land case that is just one step more complex than a water surface – relatively flat land with low vegetation. The parametrization of the turbulent fluxes for terrestrial sites and their representation in numerical models is a challenging problem because of the spatial complexity of the underlying surface especially in the case of heterogeneous or patched terrain (e.g., when bare and vegetated surfaces coexist) or for non-saturated conditions, which are common in arid and semi-arid climates, and in complex terrain (e.g. Bou-Zeid et al. 2020; Cuxart and Boone 2020). Myriad different types of climates, soils, and vegetation add extra complexity in the problem. Another issue of the flux estimates from routine meteorological measurements over land is associated with the availability of the relevant model input parameters and their related uncertainties. This implies a need to use non-traditional synthetic methods and to work in an interdisciplinary framework.

Using the data from the second Wind Forecast Improvement Project (WFIP 2) field campaign collected in the Columbia River Gorge area of irregular terrain near Wasco, Oregon, during 2016-2017, we have developed and tested an optimized hybrid bulk flux algorithm for predicting the turbulent surface fluxes of momentum, sensible, and latent heat (1)-(3) over dry and wet bare or lightly vegetated soil surfaces. The bulk flux algorithm combines (i) the traditional COARE bulk flux algorithm (Fairall et al. 1996, 2003) adopted for over-land situations for estimation of the turbulent fluxes of momentum τ and the sensible heat H_S (Section

3 and as described in the Appendix), and (ii) a modified Priestley-Taylor (P-T) model (11) with physically based ecophysiological constraints (12) by Yao et al. (2015) to estimate the latent heat flux H_L (or moisture flux) (Section 4). Whereas bulk estimates of τ and H_S are derived from a traditional approach, which is based on the transfer coefficients (drag coefficient and Stanton number), aerodynamic and scalar roughness lengths, and MOST flux-profile relationships, modeled values of H_L are evaluated from a modified P-T approach, which is essentially based on the SEB equation (4) (i.e., on the conservation of energy principle). Note also, that a MOST-based flux-profile approach or a bulk flux algorithm requires measurements of the relevant variables (e.g., wind speed and T/RH) at two different levels whereas a SEB-type model needs data (e.g., radiative fluxes) from a single level only. One may classify this approach as a hybrid or synthetic (composite) approach because it uses different physical principles for parameterization of the turbulent fluxes. Our hybrid bulk flux approach is summarized in Table 1.

Thus, the novelty in our bulk flux algorithm for a terrestrial tower site is associated with the use of a hybrid approach to predict the turbulent fluxes, when even the turbulent energy fluxes, H_S and H_L, are estimated from two completely different physical principles. As mentioned above, a two-level aerodynamic method for a turbulent flow in the case of τ and H_S estimates (i.e., a traditional bulk approach) and the first law of thermodynamics at the interface for H_L estimates (one may say that these two approaches are "apples and oranges"). In addition, a hybrid approach is characterized by flexible logic. For example, H_L can be estimated from another model based on the SEB equation (4), whereas τ and H_S can be derived from a gradient method (requiring meteorological measurements at two atmospheric levels) rather a traditional bulk approach (requiring meteorological measurements at one atmospheric level and estimation of θ_0, z_{0x} at the surface–atmosphere interface, see Section 4). Obviously other options for the flux estimates are also possible in the framework of a hybrid approach (e.g., see Basu 2019 for discussion).

In this study, we use two 30-day long uninterrupted time series of the data separately for dry and wet soil conditions (WFIP 2 "golden files"). Time periods from 27 August to 26 September 2016 (YD 240–270) and 25 March to 24 April 2017 (YD 450–480 with respect to 1 January 2016) were selected to calibrate and verify parameterizations for the surface fluxes over dry and wet soil surfaces respectively (see Grachev et al. 2020 for further detail). We sorted the data into dry and wet categories based on the soil temperature and soil moisture measured at 5 cm depth (Section 2). The direct measurements of the surface fluxes (turbulent and radiative) and other ancillary atmospheric/soil parameters made during WFIP 2 for different soil conditions (dry and wet) are used to optimize and tune the hybrid bulk algorithm. In particular, our results suggest that the P-T coefficient α varies with soil moisture according to (21). Because direct measurements of the soil heat flux G (e.g., with a heat flux plate) were not available during the field campaign WFIP 2, G in the P-T model (11) was estimated from the Fourier's Law of Heat Conduction (6) based measurements of soil temperature and soil moisture. Dependence of the thermal conductivity of the soil λ in (6) versus soil moisture content at 5 cm depth for the entire field campaign (Fig. 10) was estimated via. Eq. (21).

The bulk flux estimates have been validated against the eddy-covariance fluxes (Fig. 11). According to linear regression slopes for the scatter plots shown in Fig. 11, the bulk flux estimates for H_S and H_L predicted by the hybrid bulk flux algorithm provide reasonable agreement on average (within a few percent except H_L for the dry period) with the measured half-hourly averaged flux values (see also Tables 2 and 3). In this study we also discuss the SEB closure over dry and wet surfaces at various timescales (from half-hourly to monthly averages) based on the modelled and measured fluxes for the dry and wet soil "golden files" periods (Figs. 13 and 14). In addition, we tested the model beyond the 30-day "golden files" calibration periods without further tuning (Figs. 15 and 16). The bulk flux algorithm described in Section 4 is optimized for the data collected at the WFIP 2 Physics Site PS01. However, our model and its modifications can be used for other similar flux-tower sites and similar field campaigns.

It can be assumed that our approach is applicable to other similar sites in which advection, heterogeneity etc. is considered not to be relevant. This is because our approach is based on the first principles; that is, on the aerodynamic method for a turbulent mixing in the case of τ and H_S estimates and the first law of thermodynamics at the interface for H_L estimates. To apply our approach to other locations, the tunable model parameters associated with surface properties and soil type (e.g., z_0 and λ) must be changed. However, it is necessary to keep in mind that our approach as well as other land-surface models and remote-sensing applications assume a closed energy balance only for four main terms (4), allowing to compute explicitly missing terms as the residual of the others (e.g., Cuxart et al. 2015; Mauder et al. 2020 and references therein). The limitation of this approach is associated with neglecting of all storage and transport contributions, and other unspecified processes. This can lead to systematic bias in estimates of the energy fluxes (in our case H_L). Mauder et al. (2020) recently survey different methods of estimating the magnitude of the SEB residual imbalance, which can improve the predictability of the energy fluxes.

Acknowledgements. This work was supported by the National Oceanic and Atmospheric Administration (NOAA) Atmospheric Science for Renewable Energy (ASRE) program and by the U.S. Department of Energy (DoE) DE-EE0007605 interagency agreement that supports DoE FOA DE-FOA-0000984. The University of Notre Dame team was supported by DOE-WFIFP2-SUB-001. HJSF was also supported by NSF grants AGS-1565535 and 1921554.

APPENDIX

Turbulent Bulk Flux Algorithm

In a traditional bulk turbulent flux algorithm in Eq. (8)–(10), we make a distinction between the scalar averaged wind speed (i.e., the mean wind speed), S, and the vector averaged wind speed (i.e., the magnitude of the mean wind vector), U, at reference height z (see Grachev et al. 1998, Section 3.1, and Akylas et al. 2003, Section 2a, for discussion). The vector averaging of the wind speed first takes the average of the longitudinal and lateral wind speed components, u and v respectively, and then takes the square,

$$U = \left(\bar{u}^2 + \bar{v}^2\right)^{1/2} \qquad (A1)$$

whereas the scalar averaging firstly takes the square and then average,

$$S = \left(\overline{u^2} + \overline{v^2}\right)^{1/2} \qquad (A2)$$

Combining $(A1)$ and $(A2)$ with the definition of variance leads to a relationship between U and S:

$$S^2 - U^2 = \left(\overline{u^2} - \bar{u}^2\right) + \left(\overline{v^2} - \bar{v}^2\right) = \sigma_u^2 + \sigma_v^2 \qquad (A3)$$

where σ_u and σ_v are the horizontal velocity variances. Relationship (A3) is also known as the gustiness assumption (e.g., Fairall et al. 1996; Grachev et al. 1998). According to $(A3)$, S in such conditions is the vector sum U and the convective gustiness velocity, $U_G = (\sigma_u^2 + \sigma_v^2)^{1/2}$:

$$S^2 = U^2 + U_G^2 = (UG_f)^2 \qquad (A4)$$

where $G_f = S/U$ is called the gustiness factor. In convective conditions, large-scale circulations embracing the entire convective boundary layer (CBL) create random gusts that crucially affect the surface fluxes. In the COARE bulk algorithm, for unstable stratification $U_G = \beta w_*$ where

$\beta \approx 1.25$ (Fairall et al. 1996) and $w_* = \left(\overline{w'\theta_v{}'}gh/\theta_v\right)^{1/3}$ is the Deardorff (1970) convective velocity scale (θ_v is the virtual temperature, and h is the CBL height). A key point of ($A4$) is employment of σ_u, $\sigma_v \sim w_*$ (Panofsky et al. 1977); that is, a convective gust is proportional to the Deardorff (1970) velocity scale w_*, which is added to the mean wind speed U. Thus, under light wind conditions (in the free-convection limit) $U \to 0$ whereas $S \to w_*$. Note that variances of the horizontal wind components in the convective surface layer are practically independent of height and, therefore, do not follow the traditional surface layer scaling.

It is obvious that vector or scalar averaging can be applied to the turbulent stress as well since the instantaneous vector of the wind stress has the same direction as the wind vector (Grachev et al. 1998; Akylas et al. 2003). Similar to S defined by Eqs. ($A2$)–($A4$), the scalar averaged stress, τ_S, has a finite limit as U approaches zero. In this case, random CBL-scale coherent structures produce a local log-profile in the layer attached to the bottom of the large eddies. This local velocity profile generates a local stress (the 'minimum friction velocity'). Thus, the concept of gustiness immediately leads to a 'minimum friction velocity' assumption (e.g. Businger 1973; Schumann 1988; Sykes et al. 1993; Akylas et al. 2003) also referred as the convection-induced stress regime (Grachev et al. 1997, 1998; Zilitinkevich et al. 1998, 2005, 2006). In fact, free convection can be considered as a particular case of forced convection. Zilitinkevich et al. (1998, 2005, 2006) developed a more detailed theoretical model for the non-local momentum and heat transfer. The vector or scalar averaging of the turbulent stress is related in particular to the time averaging procedure. Mahrt et al. (1996) reported a substantial difference of the drag coefficient in light winds for different averaging times and vector/scalar wind speed averaging procedures. According to Mahrt et al. (1996), higher values of the drag coefficient occur for a 10-min time averaging period compared to 60-min averaged values. The vector averaging of the surface stress would be appropriate for determination of the average, net large scale force acting on a surface (e.g., for description of the surface currents for measurements over sea surface). Note that both the COARE and SHEBA bulk flux algorithms as well as Eq. (8) are based on the vector averaging of the turbulent stress when $\tau = \rho u_*^2 \propto SU$ whereas the scalar averaged wind stress assumes $\tau_S = \rho u_{*S}^2 \propto S^2$ (where u_{*S} is the friction velocity based on the scalar averaging).

The COARE bulk flux algorithm is described in detail by Fairall et al. (1996, 2003) but it is sketched here. The transfer coefficients in (8)–(10) are partitioned into individual profile components (Fairall et al. 1996, Eq. 5):

$$C_D = c_d^{1/2} c_d^{1/2}, \qquad C_H = c_d^{1/2} c_h^{1/2}, \qquad C_E = c_d^{1/2} c_e^{1/2} \tag{A5}$$

The bulk variables are used to compute so-called Monin-Obukhov (MO) scaling parameters (Fairall et al. 1996, Eq. 9):

$$u_*^2 = C_D S U, \qquad \theta_* = -c_h^{\frac{1}{2}} \Delta\theta, \quad q_* = -c_e^{\frac{1}{2}} \Delta q \tag{A6}$$

Traditionally, the transfer coefficients ($A6$) are adjusted to neutral conditions using MO similarity theory via (e.g., Fairall et al. 1996, Eq. 6)

$$c_d^{1/2} = \frac{c_{dn}^{1/2}}{1 - \frac{c_{dn}^{1/2}}{\kappa} \Psi_m(\zeta)}, \quad c_h^{1/2} = \frac{c_{hn}^{1/2}}{1 - \frac{c_{hn}^{1/2}}{\kappa} \Psi_h(\zeta)}, \quad c_e^{1/2} = \frac{c_{en}^{1/2}}{1 - \frac{c_{en}^{1/2}}{\kappa} \Psi_h(\zeta)} \tag{A7}$$

Here $\Psi_m(\zeta)$ and $\Psi_h(\zeta)$ are the MO profile functions for mean profiles of wind speed and scalars in the surface layer, $\kappa \approx 0.4$ is the von Kármán constant. In neutral conditions ($\zeta \equiv 0$) the Ψ-functions obey $\Psi_m(\zeta) = \Psi_h(0) = 0$. Subscript n in c_{dn}, c_{hn}, and c_{en} in ($A7$) denotes the value in neutral conditions. The MO stability parameter $\zeta = z/L$ (L is the Obukhov length) is defined by

$$\zeta = \frac{\kappa g z}{\theta_a} \frac{\theta_{v*}}{u_*^2} \tag{A8}$$

Here g is the acceleration due to gravity and, historically, the von Kármán constant is included in the definition of L and ζ simply by convention. Subscript v in θ_{v*} in $(A8)$ denotes the virtual temperature. The neutral transfer coefficients in $(A7)$ are uniquely related to the aerodynamic, z_0, and scalar, $z_{0\theta}$ and z_{0q}, roughness lengths through

$$c_{dn}^{1/2} = \frac{\kappa}{\log(z/z_0)}, \quad c_{hn}^{1/2} = \frac{\kappa}{\log(z/z_{0\theta})}, \quad c_{en}^{1/2} = \frac{\kappa}{\log(z/z_{0q})} \tag{A9}$$

The transfer coefficients depend on height via $(A9)$ but the roughness lengths are fixed for a given surface. Traditionally the transfer coefficients for operational or practical considerations are also represented at a standard reference height of 10 m and neutral conditions and denoted as C_{D10n}, C_{H10n}, and C_{E10n}. These 10-m neutral transfer coefficients are computed from U_{10n}, $\Delta\theta_{10n}$ and Δq_{10n} (see Fairall et al. 2003, Eqs. 31 and 32).

REFERENCES

Akylas E., Tsakos Y., Tombrou M., Lalas D.P., 2003: Considerations on minimum friction velocity. *Quart. J. Roy. Meteorol. Soc.* **129**(591B): 1929–1943. https://doi.org/10.1256/qj.01.73

Andreas E.L, Horst T.W., Grachev A.A., Persson P.O.G., Fairall C.W., Guest P.S., Jordan R.E., 2010a: Parametrizing turbulent exchange over summer sea ice and the marginal ice zone. *Quart. J. Roy. Meteorol. Soc.* **136**(649B), 927–943. https://doi.org/10.1002/qj.618

Andreas E.L, Persson P.O.G., Jordan R.E., Horst T.W., Guest P.S., Grachev A.A., Fairall C.W., 2010b: Parameterizing turbulent exchange over sea ice in winter. *J. Hydrometeorol*. **11**(1), 87–104. https://doi.org/10.1175/2009JHM1102.1

Assouline S., Li D., Tyler S., Tanny J., Cohen S., Bou-Zeid E., Parlange M., Katul G.G., 2016: On the variability of the Priestley- Taylor coefficient over water bodies. *Water Resour. Res*. **52**(1): 150– 163. https://doi.org/10.1002/2015WR017504

Bariteau L., Helmig D., Fairall C.W., Hare J.E., Hueber J., Lang E.K., 2010: Determination of oceanic ozone deposition by ship-borne eddy covariance flux measurements. *Atmos. Meas. Tech*. **3**(2): 441–455. https://doi.org/10.5194/amt-3-441-2010

Bianco L., Djalalova I.V., Wilczak J.M., Olson J.B., Kenyon J.S., Choukulkar A., Berg L., Fernando H.J.S., Grimit E.P., Krishnamurthy R., Lundquist J.K., Muradyan P., Pekour M., Pichugina Y., Stoelinga M.T., Turner D.D., 2019: Impact of model improvements on 80-m wind speeds during the second Wind Forecast Improvement Project (WFIP2). *Geosci. Model Dev.* **12**(11): 4803–4821. https://doi.org/10.5194/gmd-2019-80

Blomquist B.W., Huebert B.J., Fairall C.W., Bariteau L., Edson J.B., Hare J.E., McGillis W.R., 2014: Advances in air-sea CO_2 flux measurement by eddy correlation. *Boundary-Layer Meteorol*. **152**(3): 245–276. https://doi.org/10.1007/s10546-014-9926-2

Bou-Zeid E, Anderson W., Katul G.G., Mahrt L., 2020: The persistent challenge of surface heterogeneity in boundary-layer meteorology: A review. *Boundary-Layer Meteorol*. **177**(2-3): 227–245. https://doi.org/10.1007/s10546-020-00551-8

Businger J.A., 1973: A note on free convection. *Boundary-Layer Meteorol*. **4**(1-4): 323–326. https://doi.org/10.1007/BF02265241

Basu S., 2019: Hybrid profile-gradient approaches for the estimation of surface fluxes. *Boundary-Layer Meteorol*. **170**(1): 29–44. https://doi.org/10.1007/s10546-018-0391-1

Cava D., Contini D., Donateo A., Martano P., 2008: Analysis of short-term closure of the surface energy balance above short vegetation. *Agric. Forest Meteorol*. **148**(1): 82–93. https://doi.org/10.1016/j.agrformet.2007.09.003

Cristea N.C., Kampf S.K., Burges S.J., 2013: Revised coefficients for Priestley-Taylor and Makkink-Hansen equations for estimating daily reference evapotranspiration. *J. Hydrol. Eng*. **18**(10): 1289–1300. https://doi.org/10.1061/(ASCE)HE.1943-5584.0000679

Cuxart J., Boone A.A., 2020: Evapotranspiration over land from a boundary-layer meteorology perspective. *Boundary-Layer Meteorol*. **177**(2-3): 427–459. https://doi.org/10.1007/s10546-020-00550-9

Cuxart J., Conangla L., Jiménez M.A., 2015: Evaluation of the surface energy budget equation with experimental data and the ECMWF model in the Ebro Valley. *J. Geophys. Res. Atmos*. **120**(D3): 1008–1022. https://doi.org/10.1002/2014JD022296.

De Bruin H.A.R., 1983: A model for the Priestley-Taylor parameter α. *J. Climate Appl. Meteor*. **22**(4): 572–578. https://doi.org/10.1175/1520-0450(1983)022<0572:AMFTPT>2.0.CO;2

De Bruin H.A.R., Holtslag A.A.M., 1982: A simple parameterization of the surface fluxes of sensible and latent heat during daytime compared with the Penman-Monteith concept. *J. Appl. Meteor*. **21**(11): 1610–1621. https://doi.org/10.1175/1520-0450(1982)021<1610:ASPOTS>2.0.CO;2

Fairall C.W., Bradley E.F., Rogers D.P., Edson J.B., Young G.S., 1996: Bulk parameterization of air-sea fluxes for Tropical Ocean - Global Atmosphere Coupled-Ocean Atmosphere Response Experiment. *J. Geophys. Res.* **101**(C2): 3747–3764. https://doi.org/10.1029/95JC03205

Fairall C.W., Bradley E.F., Hare J.E., Grachev A.A., Edson J.B., 2003: Bulk parameterization of air-sea fluxes: updates and verification for the COARE algorithm. *Journal of Climate*, **16**(4), 571–591.

Fisher J.B., Tu K.P., Baldocchi D.D., 2008: Global estimates of the land–atmosphere water flux based on monthly AVHRR and ISLSCP-II data, validated at 16 FLUXNET sites. *Remote Sens. Environ.* **112**(3): 901-919. https://doi.org/10.1016/j.rse.2007.06.025

Foken T., Wimmer F., Mauder M., Thomas C., Liebethal C., 2006: Some aspects of the energy balance closure problem. *Atmos. Chem. Phys*. **6**(12): 4395–4402. https://doi.org/10.5194/acp-6-4395-2006

Foken T., 2008: The energy balance closure problem: An overview. *Ecological Applications*, **18**(6): 1351–1367. https://doi.org/10.1890/06-0922.1

Foken T., 2017: *Micrometeorology.* Second Edition, Springer-Verlag, Berlin Heidelberg, 362 p. https://doi.org/10.1007/978-3-642-25440-6

Gao Z., Liu H., Katul G.G., Foken T., 2017a: Non-closure of the surface energy balance explained by phase difference between vertical velocity and scalars of large atmospheric eddies. *Environ. Res. Lett*. **12**(3): 034025. https://doi.org/10.1088/1748-9326/aa625b

Gao Z., Russell E.S., Missik J.E.C., Huang M., Chen X., Strickland C.E., Clayton R., Arntzen E., Ma Y., Liu H., 2017b: A novel approach to evaluate soil heat flux calculation: An analytical review of nine methods. *J. Geophys. Res*. **122**(D3): 6934–6949. https://doi.org/10.1002/2017JD027160

Garratt J.R., 1992: *The Atmospheric Boundary Layer.* Cambridge University Press, U.K. 316 pp

Grachev A.A., Fairall C.W., Zilitinkevich S.S., 1997: Surface-layer scaling for the convection-induced stress regime. *Boundary-Layer Meteorol*. **83**(3), 423–439. https://doi.org/10.1023/A:1000281625985

Grachev A.A., Fairall C.W., Larsen S.E., 1998: On the determination of the neutral drag coefficient in the convective boundary layer. *Boundary-Layer Meteorol*. **86**(2): 257–278. https://doi.org/10.1023/A:1000617300732

Grachev A.A., Bariteau L., Fairall C.W., Hare J.E., Helmig D., Hueber J., Lang E.K., 2011: Turbulent fluxes and transfer of trace gases from ship-based measurements during TexAQS 2006. *J. Geophys. Res.* **116**: D13110. https://doi.org/10.1029/2010JD015502

Grachev A.A., Andreas E.L, Fairall C.W., Guest P.S., Persson P.O.G., 2015: Similarity theory based on the Dougherty-Ozmidov length scale. *Quart. J. Roy. Meteorol. Soc.* **141**(690A): 1845–1856. https://doi.org/10.1002/qj.2488

Grachev A.A., Fairall C.W., Blomquist B.W., Fernando H.J.S., Leo L.S., Otárola-Bustos S.F., Wilczak J.M., McCaffrey K.L., 2020: On the surface energy balance closure at different temporal scales. *Agric. Forest Meteorol.* **281**: https://doi.org/10.1016/j.agrformet.2019.107823

Hao Y., Baik J., Choi M., 2019: Developing a soil water index-based Priestley–Taylor algorithm for estimating evapotranspiration over East Asia and Australia. *Agric. Forest Meteorol*. **279**: https://doi.org/10.1016/j.agrformet.2019.107760

Higgins C.W., 2012: A-posteriori analysis of surface energy budget closure to determine missed energy pathways. *Geophys. Res. Lett*. **39**(19): L19403. https://doi.org/10.1029/2012GL052918

Jacobs A.F.G., Heusinkveld B.G., Holtslag A.A.M., 2008: Towards closing the surface energy budget of a mid-latitude grassland. *Boundary-Layer Meteorol*. **126**(1): 125–136. https://doi.org/10.1007/s10546-007-9209-2

Kondo J., Saigusa N., Sato T., 1990: A parameterization of evaporation from bare soil surfaces. J. Appl. Meteor. 29(5): 385–389.

Kustas W.P., Daughtry C.S.T., Van Oevelen P.J., 1993: Analytical treatment of the relationship between soil heat flux/net radiation ratio and vegetation indices. *Remote Sens. Environ*. **46**(3): 319–330. https://doi.org/10.1016/0034-4257(93)90052-Y

Kustas W.P., Norman J.M., Schmugge T.J., Anderson M.C., 2004: Mapping surface energy fluxes with radiometric temperature. In: D.A. Quattrochi, J.C. Luvall (eds.) *Thermal remote sensing in land surface processes*. Boca Raton, Florida: CRC Press, 2004, p. 205–253.

Lhomme J.A., 1997: A theoretical basis for the Priestley-Taylor coefficient. *Boundary-Layer Meteorol*. 82(2): 179–191. https://doi.org/10.1023/A:1000281114105

Leuning R., van Gorsel E., Massman W.J., Isaac P.R., 2012: Reflections on the surface energy imbalance problem. *Agric. Forest Meteorol*. **156**: 65–74. https://doi.org/10.1016/j.agrformet.2011.12.002

Li Z.L., Tang R.L., Wan Z.M., Bi Y.Y., Zhou C.H., Tang B.H., Yan G.J., Zhang X.Y., 2009: A review of current methodologies for regional evapotranspiration estimation from remotely sensed data. *Sensors*. **9**(5): 3801-3853. https://doi.org/10.3390/s90503801

Liebethal C., Foken T., 2007. Evaluation of six parameterization approaches for the ground heat flux. *Theor. Appl. Climatol*. **88**(1-2): 43–56. https://doi.org/10.1007/s00704-005-0234-0

Liebethal C., Huwe B., Foken T., 2005: Sensitivity analysis for two ground heat flux calculation approaches. *Agric. For. Meteorol*. **132**(3-4): 253–262. https://doi.org/10.1016/j.agrformet.2005.08.001

Mahrt L., Vickers D., Howell J., Højstrup J., Wilczak J. M., Edson J., Hare J., 1996: Sea surface drag coefficients in the Risø Air Sea Experiment. *J. Geophys. Res*. **101**(C6): 14,327–14,335. https://doi.org/10.1029/96JC00748

Majozi N.P., Mannaerts C.M., Ramoelo A., Mathieu R., Nickless A., Verhoef W., 2017: Analysing surface energy balance closure and partitioning over a semi-arid savanna FLUXNET site in Skukuza, Kruger National Park, South Africa. *Hydrol. Earth Syst. Sci*. **21**(7): 3401–3415. https://doi.org/10.5194/hess-21-3401-2017

Mauder M., Oncley S.P., Vogt R., Weidinger T., Ribeiro L., Bernhofer C., Foken T., Kohsiek W., De Bruin H.A.R., Liu H., 2007: The Energy Balance Experiment EBEX-2000. Part II: Intercomparison of eddy-covariance sensors and post-field data processing methods. *Boundary-Layer Meteorol*. **123**(1): 29–54. https://doi.org/10.1007/s10546-006-9139-4

Mauder M., Foken T., Cuxart J., 2020: Surface-energy-balance closure over land: A review. *Boundary-Layer Meteorol.* **177**(2-3): 395–426. https://doi.org/10.1007/s10546-020-00529-6

Masseroni D., Corbari C., Mancini M., 2014: Limitations and improvements of the energy balance closure with reference to experimental data measured over a maize field. *Atmósfera*, **27**(4): 335–352. https://doi.org/10.1016/S0187-6236(14)70033-5

Meyers T.P., Hollinger S.E., 2004: An assessment of storage terms in the surface energy balance of maize and soybean. *Agric. Forest Meteorol*. **125**(1-2): 105–115. https://doi.org/10.1016/j.agrformet.2004.03.001

Monteith J.L., 1965: Evaporation and Environment. In: The state and movement of water in living organism. *19th Symp. Soc. Exptl. Biol*. 205–234.

Olson J.B., Kenyon J.S., Djalalova I., Bianco L., Turner D.D., Pichugina Y., Chokulkar A., Toy M.D., Brown J.M., Angevine W.M., Akish E., Bao J.-W., Jimenez P., Kosović B., Lundquist K.A., Draxl C., Lundquist J.K., McCaa J., McCaffrey K., Lantz K., Long C., Wilczak J., Banta R., Marquis M., Redfern S., Berg L.K., Shaw W., Cline J., 2019: Improving wind energy forecasting through numerical weather prediction model development. *Bull. Amer. Meteorol. Society*. **100**(11): 2201–2220. https://doi.org/10.1175/BAMS-D-18-0040.1

Oncley S.P., Foken T., Vogt R., Kohsiek W., DeBruin H.A.R., Bernhofer C., Christen A., van Gorsel E., Grantz D., Feigenwinter C., Lehner I., Liebethal C., Liu H., Mauder M., Pitacco A., Ribeiro L., Weidinger T., 2007: The energy balance experiment EBEX-2000, Part I: Overview and energy balance. *Boundary Layer Meteorol*. **123**(1): 1–28. https://doi.org/10.1007/s10546-007-9161-1

Penman H.L., 1948: Natural evaporation from open water, bare soil and grass. *Proceedings of the Royal Society of London*. Series A, Mathematical and Physical Sciences, **193**(1032): 120–145.

Pereira A.R., 2004: The Priestley-Taylor parameter and the decoupling factor for estimating reference evapotranspiration. *Agric. Forest Meteorol*. **125**(3-4): 305–313. https://doi.org/10.1016/j.agrformet.2004.04.002

Priestley C. and Taylor R., 1972. On the assessment of surface heat flux and evaporation using large-scale parameters. *Mon. Wea. Rev*. **100**(2): 81–92.

Schumann U., 1988: Minimum friction velocity and heat transfer in the rough surface layer of a convective boundary layer. *Boundary-Layer Meteorol*. **44** (4): 311–326. https://doi.org/10.1007/BF00123019

Shaw W., Berg L., Cline J., Draxl C., Djalalova I., Grimit E., Lundquist J.K., Marquis M., McCaa J., Olson J., Sivaraman C., Sharp J., Wilczak J.M., 2019: The second Wind Forecast Improvement Project (WFIP2): General overview. *Bull. Amer. Meteorol. Society*. **100**(9): 1687–1699. https://doi.org/10.1175/BAMS-D-18-0036.1

Stoy P.C., Mauder M., Foken T., Marcolla B., Boegh E., Ibrom A., Arain M.A., Arneth A., Aurela M., Bernhofer C., Cescatti A., Dellwik E., Duce P., Gianelle D., van Gorsel E., Kiely G., Knohl A., Margolis H., McCaughey H., Merbold L., Montagnani L., Papale D., Reichstein M., Saunders M., Serrano-Ortiz P., Sottocornola M., Spano D., Vaccari F., Varlagin A., 2013: A data-driven analysis of energy balance closure across FLUXNET research sites: The role of landscape scale heterogeneity. *Agric. Forest Meteorol*. **171-172**: 137–152. https://doi.org/10.1016/j.agrformet.2012.11.004

Su Z., 2002: The Surface Energy Balance System (SEBS) for estimation of turbulent heat fluxes. *Hydrol. Earth Syst. Sci*. **6**(1): 85–100. https://doi.org/10.5194/hess-6-85-2002

Sykes R.I., Henn D.S., Lewellen W.S., 1993: Surface-layer description under free-convection conditions. *Quart. J. Roy. Meteorol. Soc*. **119**(511): 409–421. https://doi.org/10.1002/qj.49711951103

Venturini V., Rodriguez L., Bisht G., 2011: Comparison among different modified Priestley and Tayor equations to calculate actual evapotranspiration with MODIS data. *Int. J. Remote Sens*. **32**(5): 1319–1338. https://doi.org/10.1080/01431160903547965

Wilson K., Goldstein A., Falge E., Aubinet M., Baldocchi D., Berbigier P., Bernhofer C., Ceulemans R., Dolman H., Field C., Grelle A., Ibrom A., Law B.E, Kowalski A., Meyers T., Moncrieff J., Monson R., Oechel W., Tenhunen J., Valentini R., Verma S., 2002: Energy balance closure at FLUXNET sites. *Agric. Forest Meteorol*. **113**(1-4): 223–243. https://doi.org/10.1016/S0168-1923(02)00109-0

Wilczak J.M., Oncley S.P., Stage S.A., 2001: Sonic anemometer tilt correction algorithms. *Boundary-Layer Meteorol.* **99**(1): 127–150. https://doi.org/10.1023/A:1018966204465

Wilczak J.M., Stoelinga M., Berg L., Sharp J., Draxl C., McCaffrey K., Banta R.M., Bianco L., Djalalova I., Lundquist J.K., Muradyan P., Choukulkar A., Leo L., Bonin T., Pichugina Y., Eckman R., Long C., Lantz K., Worsnop R., Bickford J., Bodini N., Chand D., Clifton A., Cline J., Cook D., Fernando H.J.S., Friedrich K., Krishnamurthy R., Marquis M., McCaa J., Olson J., Otarola-Bustos S., Scott G., Shaw W.J., Wharton S., White A.B., 2019: The second Wind Forecast Improvement Project (WFIP2): Observational field campaign. *Bull. Amer. Meteorol. Society*. **100**(9): 1701–1723. https://doi.org/10.1175/BAMS-D-18-0035.1

Yaglom A.M., 1974: Data on turbulence characteristics in the atmospheric surface layer. Izvestiya, Acad.Sci., USSR, Atmos. Oceanic Phys. 10: 341–352.

Yao Y., Liang S., Cheng J., Liu S., Fisher J. B., Zhang X., Jia K., Zhao X., Qin Q., Zhao B., Han S., Zhou G., Zhou G., Li Y., Zhao S., 2013: MODIS-driven estimation of terrestrial latent heat flux in China based on a modified Priestley-Taylor algorithm. *Agric. Forest Meteorol*. **171–172**: 187–202. https://doi.org/10.1016/j.agrformet.2012.11.016

Yao Y., Liang S., Zhao S., Zhang, Y., Qin Q., Cheng J., Jia K., Xie X., Zhang N., Liu M., 2014: Validation and application of the modified satellite-based Priestley-Taylor algorithm for mapping terrestrial evapotranspiration. *Remote Sens*. **6**(1): 880–904. https://doi.org/10.3390/rs6010880

Yao Y., Liang S., Li X., Chen J., Wang K., Jia K., Cheng J., Jiang B., Fisher J.B., Mu Q., Grünwald T., Bernhofer C., Roupsard O., 2015: A satellite-based hybrid algorithm to determine the Priestley-Taylor parameter for global terrestrial latent heat flux estimation across multiple biomes. *Remote Sens. Environ*. **165**: 216–233. https://doi.org/10.1016/j.rse.2015.05.013

Zilitinkevich S.S., Grachev A.A., Hunt J.C.R. 1998: Surface frictional and non-local heat/mass transfer in the shear-free convective boundary layer, in *Buoyant Convection in Geophysical Flows* (Plate E.J., Fedorovich E.E., Viegas D.X., Wyngaard J.C., Eds.), NATO ASI Series (Series C: Mathematical and Physical Sciences), vol. **513**: 83–113. Kluwer/Springer, Dordrecht, the Netherlands. https://doi.org/10.1007/978-94-011-5058-3_4

Zilitinkevich S.S., Hunt J.C.R., Grachev A.A., Esau I.N., Lalas D.P., Akylas E., Tombrou M., Fairall C.W., Fernando H.J.S., Baklanov A., Joffre S.M., 2005: The effect of large eddies on the convective heat/mass transfer over complex terrain: advanced theory and its validation against experimental and les data. *Croatian Meteorological Journal*. **40**, 20–26.

Zilitinkevich S.S., Hunt J.C.R., Esau I.N., Grachev A.A., Lalas D.P., Akylas E., Tombrou M., Fairall C.W., Fernando H.J.S., Baklanov A.A., Joffre S.M., 2006: The influence of large convective eddies on the surface layer turbulence. *Quart. J. Roy. Met. Soc.*, **132**(618A), 1423–1456. https://doi.org/10.1256/qj.05.79

TABLE 1. The hybrid bulk flux algorithm parameters and equations.

Flux Variables	Equations	Coefficients	Input Variables
$\tau,\ H_S$	$(A1)$, $(A2)$, (A7)	C_D, C_H	$U, \theta_0, \theta_a, q_a$
H_L	(8), (9)	α, k_i	R_{net}, G
G	(12)	λ, ρ_S, c_{pS}	θ_0, T_{S5}

TABLE 2. Summary of flux statistics (monthly averages and standard deviations) for the dry soil "golden files" (year days 240–270).

Flux Variables	<Bulk>	<Direct>	σ Bulk	σ Direct
$G\ [Wm^{-2}]$	-2.4		58.9	
$H_S\ [Wm^{-2}]$	71.5	69.9	131.2	126.9
$H_L\ [Wm^{-2}]$	9.0	7.4	20.0	22.3
$\tau\ [Nm^{-2}]$	0.10	0.12	0.11	0.13
$R_{net}\ [Wm^{-2}]$		72.8		173.0

TABLE 3. Summary of flux statistics (monthly averages and standard deviations) for the wet soil "golden files" (year days 450–480).

Flux Variables	<Bulk>	<Direct>	σ Bulk	σ Direct
$G\ [Wm^{-2}]$	7.4		66.4	
$H_S\ [Wm^{-2}]$	40.0	40.2	87.4	88.0
$H_L\ [Wm^{-2}]$	45.7	53.3	68.1	61.2
$\tau\ [Nm^{-2}]$	0.13	0.15	0.16	0.19
$R_{net}\ [Wm^{-2}]$		108.9		201.9

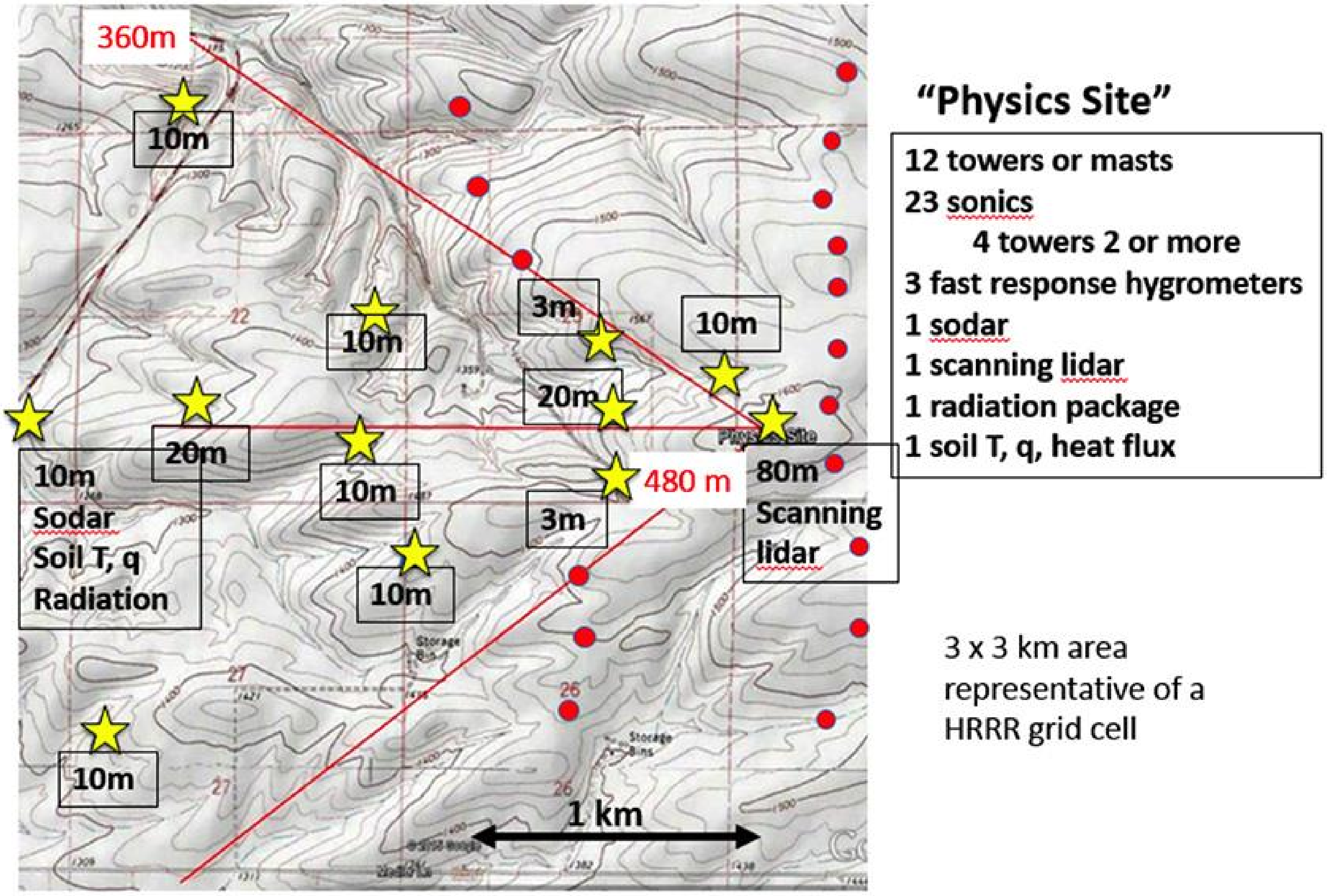

Fig. 1. Elevation map showing the Physics site with a terrain contour. Red dots are wind turbine locations; yellow stars are instrumented towers (3–20 m tall). The leftmost yellow star in the center indicates location of the 10-m PS01 flux tower. Oblique red lines indicate the angle of flow unobstructed by wind turbines for the prevailing westerly wind direction.

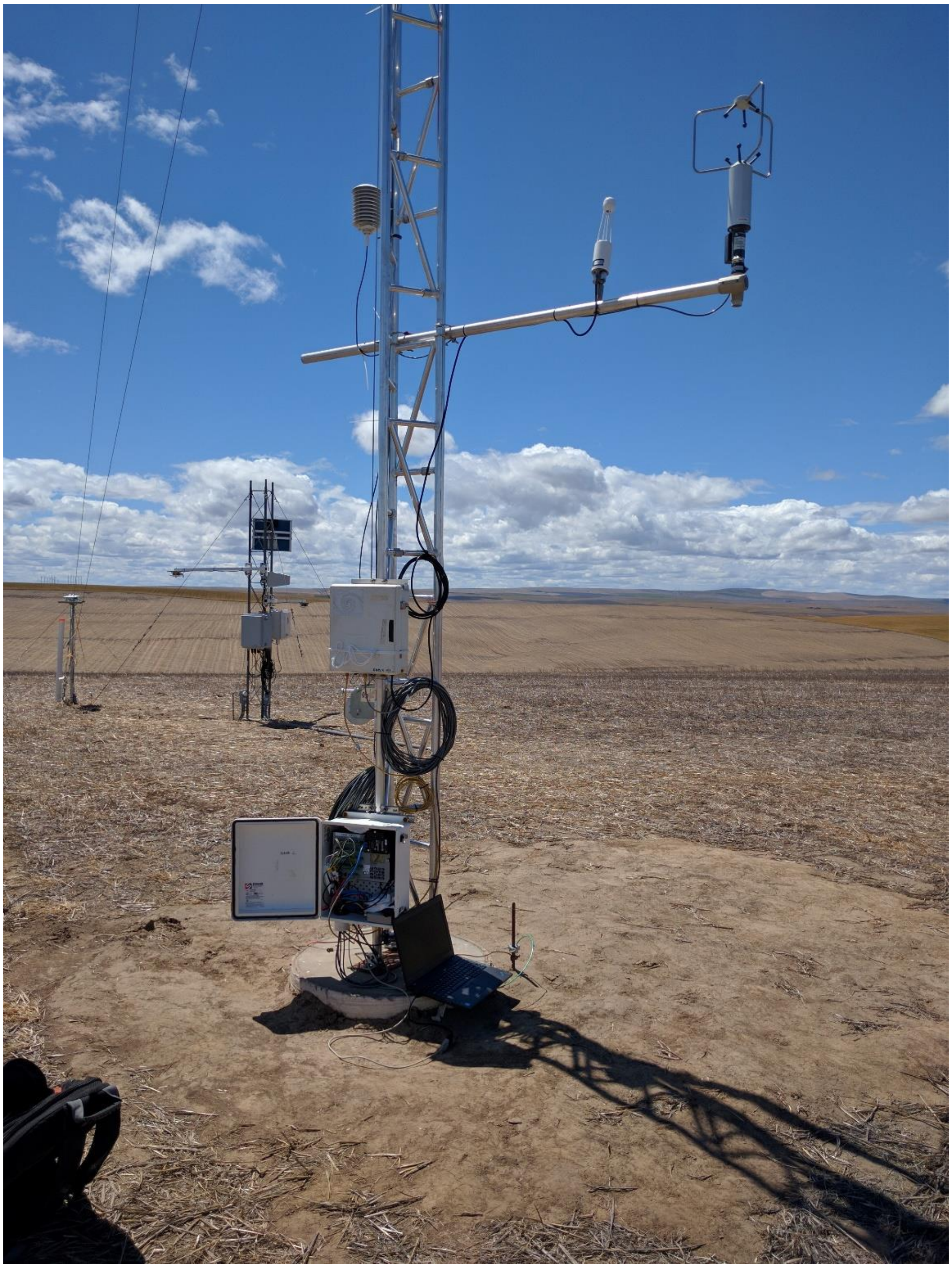

Fig. 2. View of the 10-m PS01 flux tower showing the lower (3 m) measurement level during summer conditions (23 June 2016). The two radiation masts for measurements of the downwelling and upwelling radiation are located right behind the flux tower in this photo.

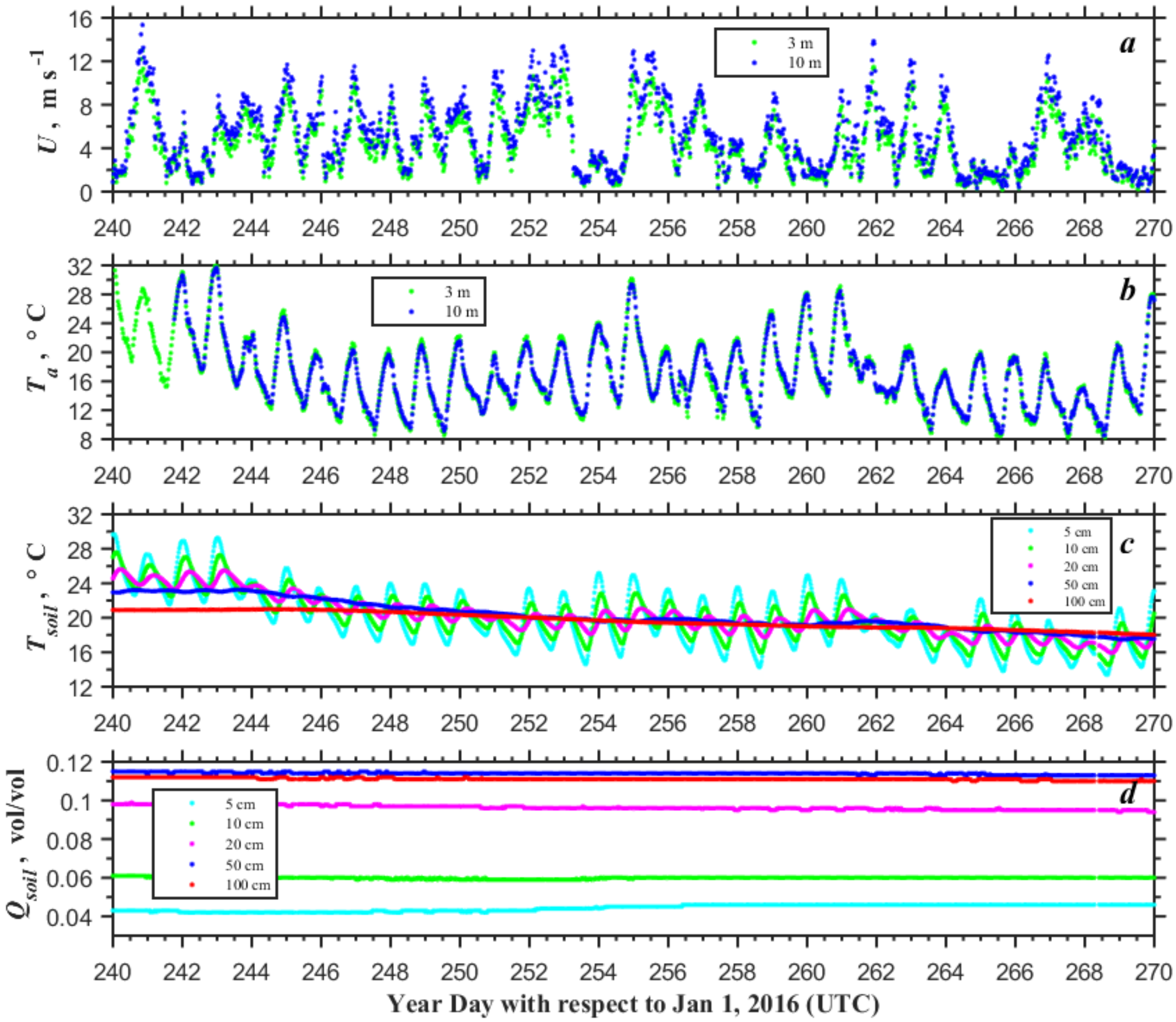

Fig. 3. One-month (30-day) time series of (*a*) wind speed, (*b*) air temperature, (*c*) soil temperature, and (*d*) volumetric soil moisture observed at the WFIP 2 Physics site PS01 during year days 240–270 (27 August-26 September 2016). The data are based on half-hour averaging.

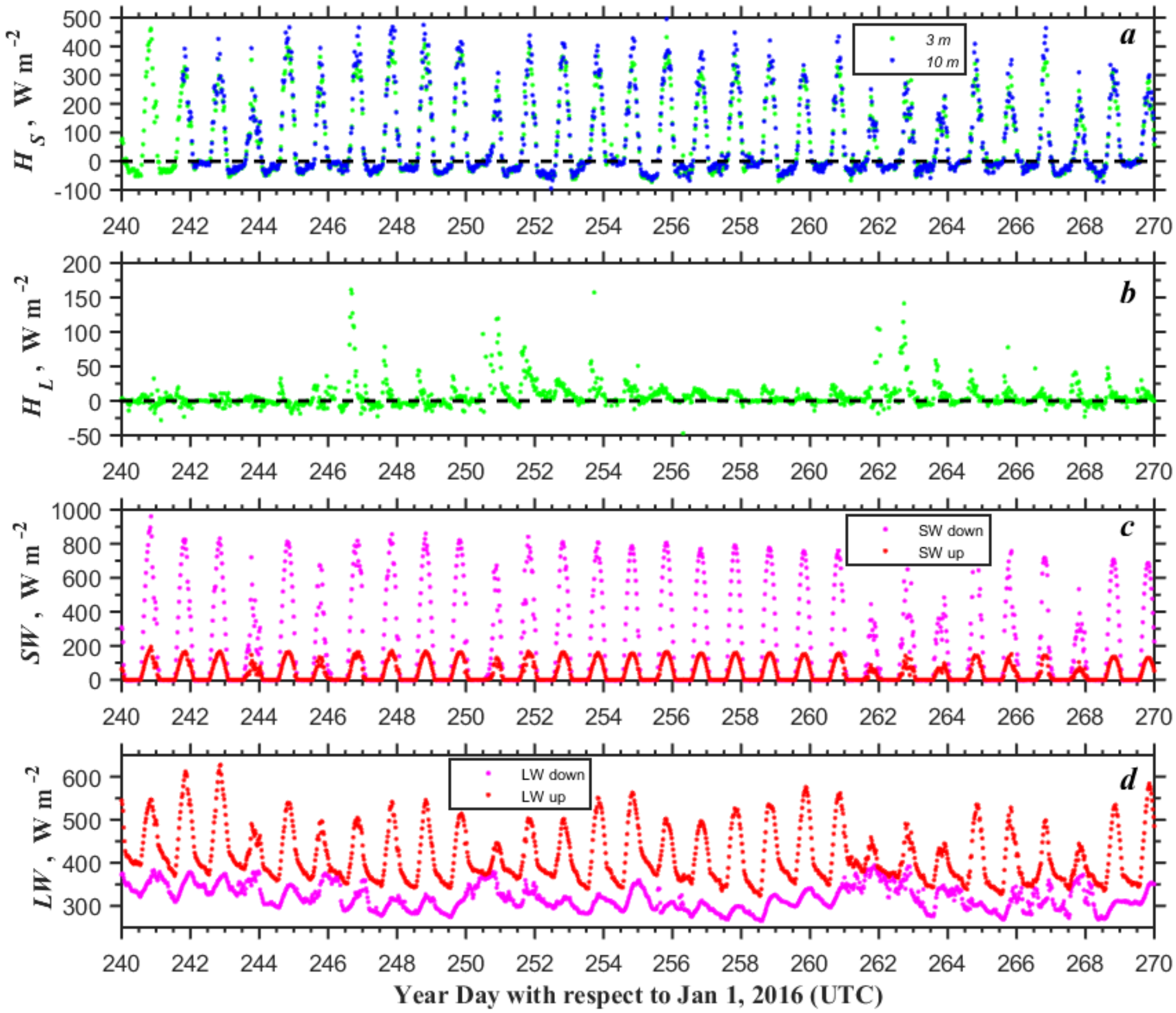

Fig. 4. One-month (30-day) time series of (*a*) sensible heat flux measured at 3 and 10 m, (*b*) latent heat (water vapor) flux measured at 3 m, (*c*) short-wave (SW) downwelling and upwelling radiation, and (*d*) long-wave (LW) downwelling and upwelling radiation observed at the WFIP 2 Physics site PS01 during year days 240–270 (27 August-26 September 2016). The data are based on half-hour averaging.

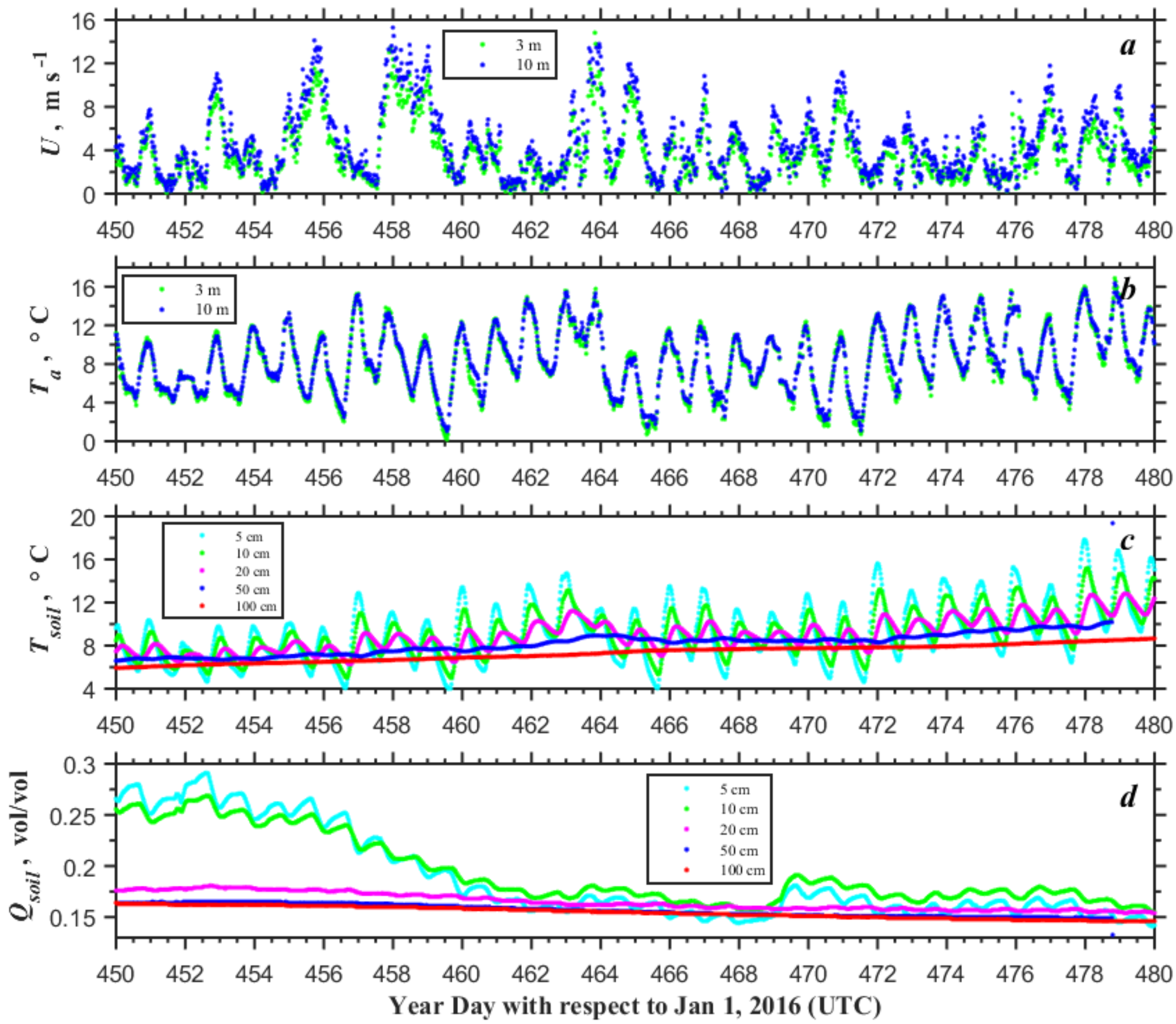

Fig. 5. Same as Fig. 3 but for wet soils observed at the WFIP 2 Physics site PS01 during year days 450–480 (25 March-24 April 2017). The data are based on half-hour averaging.

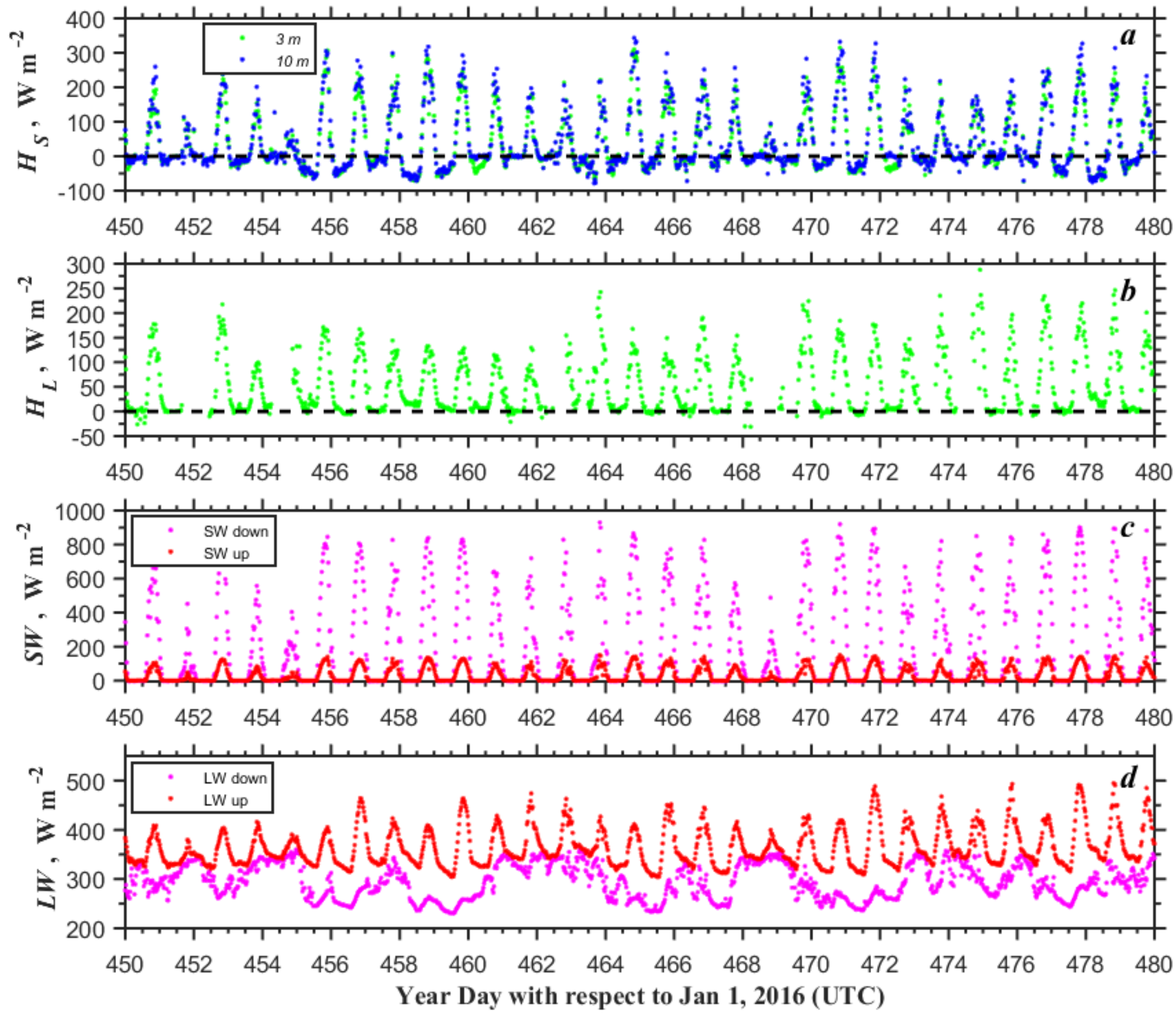

Fig. 6. Same as Fig. 4 but for wet soils observed at the WFIP 2 Physics site PS01 during year days 450–480 (25 March-24 April 2017). The data are based on half-hour averaging.

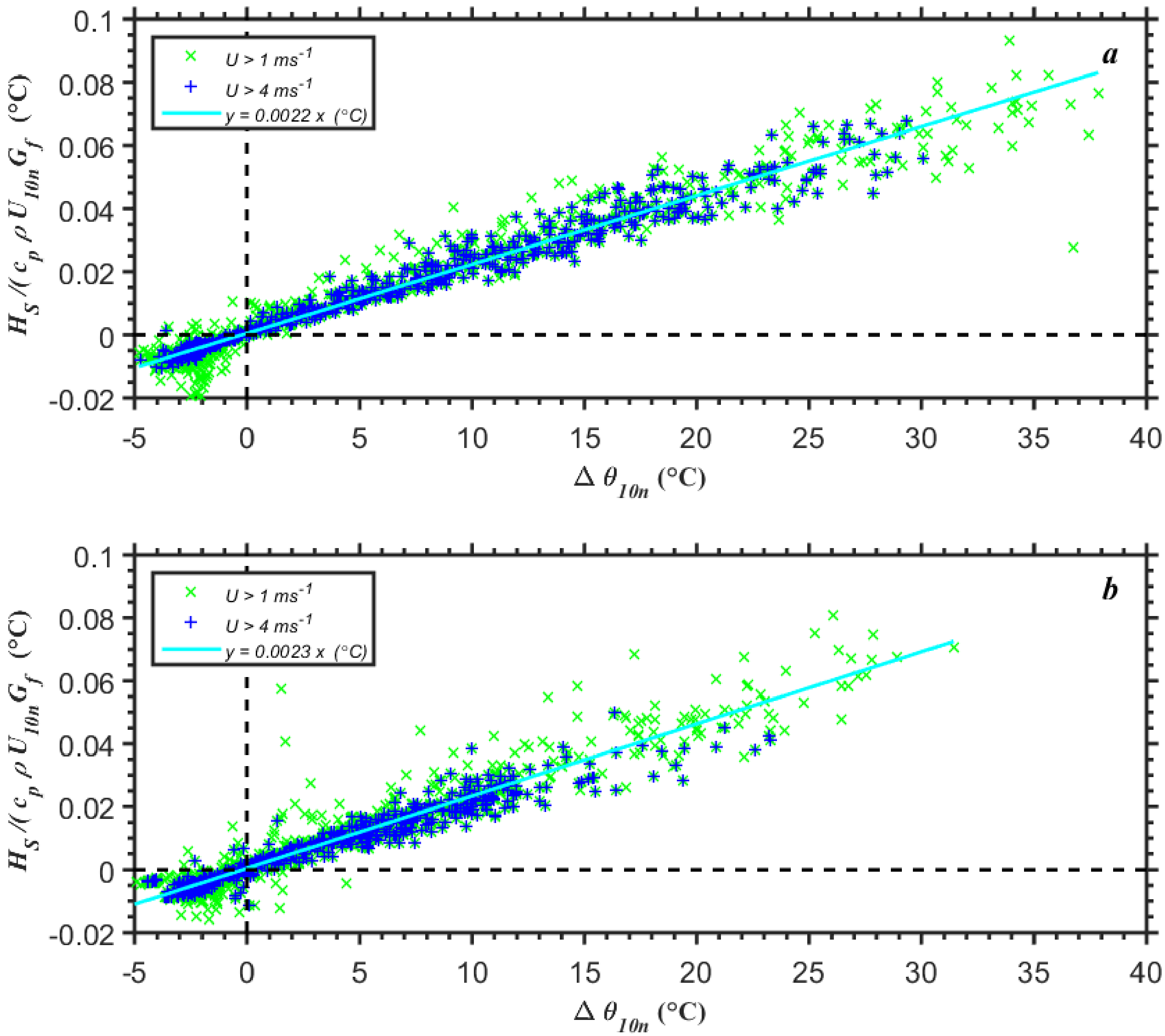

Fig. 7. Linear regression fit of half-hourly averaged covariance sensible heat flux normalized by $c_p \rho U_{10n} G_f$ versus 10-m neutral surface-air temperature difference for (*a*) the dry soil "golden files" (year days 240–270, 27 August-26 September 2016) and (*b*) the wet soil "golden files" period (year days 450–480, 25 March-24 April 2017). The green ×-symbols are data for 10-m neutral wind speed greater than 1 ms^{-1}; for blue +-symbols only wind speed greater than 4 ms^{-1} are considered. The cyan solid lines are regressions based on the half-hourly averaged values for wind speed greater than 1 ms^{-1}.

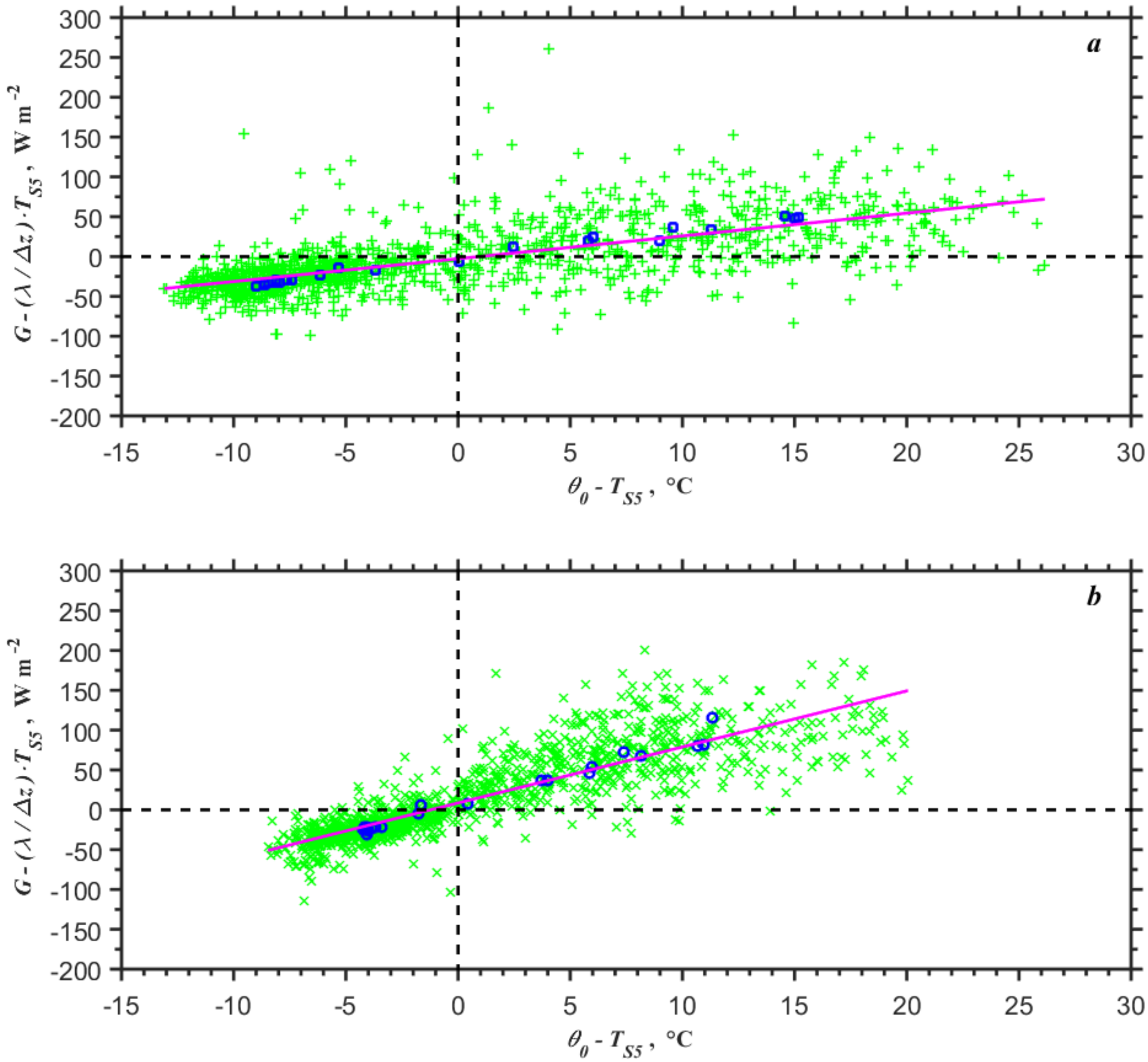

Fig. 8. The adjusted ground flux (residual) storage term versus temperature difference between surface (θ_0) and soil at 5 cm depth (T_{S5}) for (*a*) the dry soil "golden files" period (year days 240–270) and (*b*) the wet soil "golden files" period (YD 450–480). The green ×-symbols are half-hourly averaged values; blue circles are derived from the mean diurnal cycle. The magenta solid lines are regressions with $\lambda/\Delta z$ = 2.859Wm^{-2}K^{-1} for the dry soils and $\lambda/\Delta z$ = 7.034Wm^{-2}K^{-1} for the wet soils based on the half-hourly averaged values.

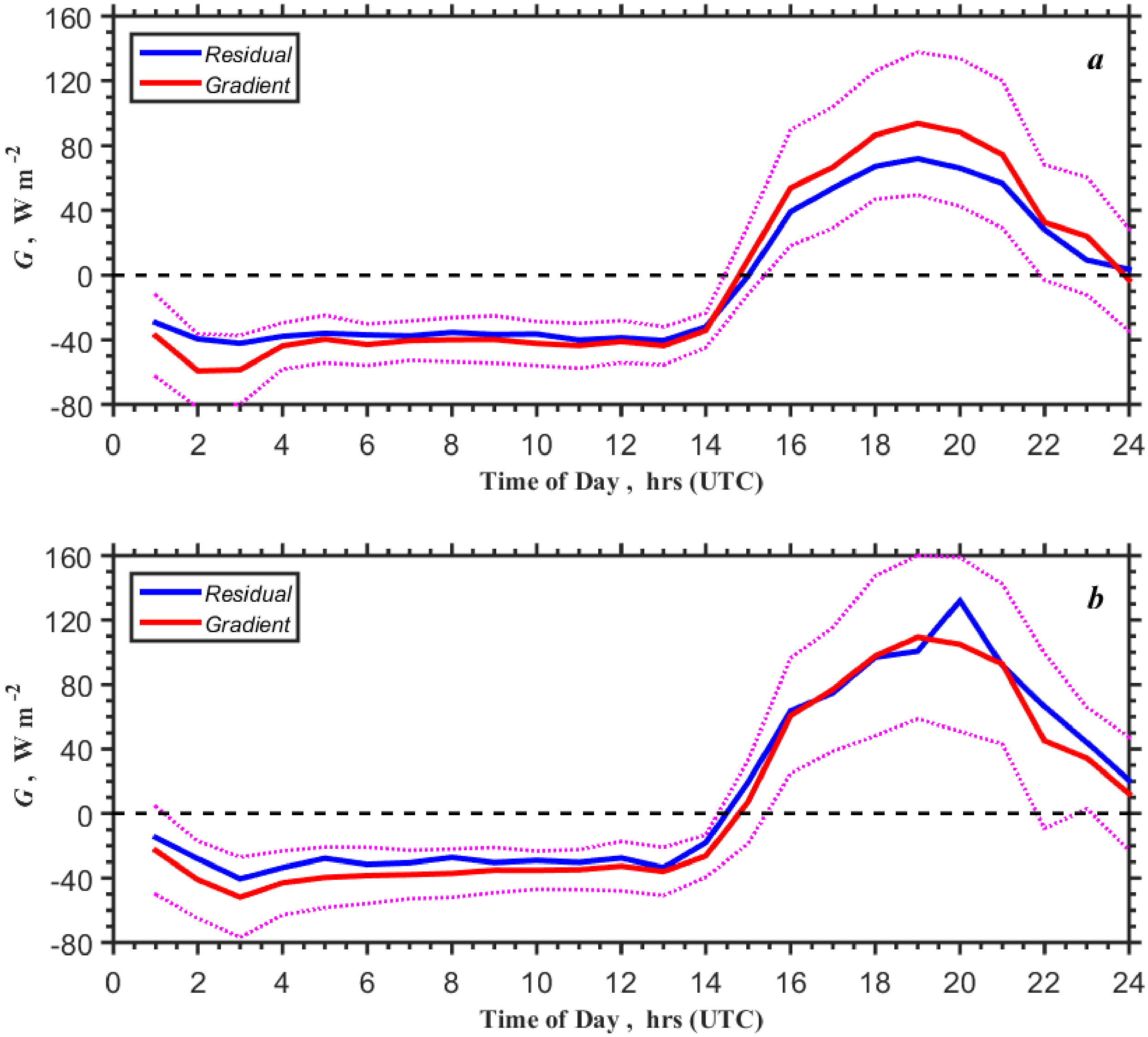

Fig. 9. Mean diurnal plot of ground flux G for (a) the dry soil "golden files" period (year days 240–270) and (b) the wet soil "golden files" period (YD 450–480). The blue lines are the residual estimate of G and the red lines are G computed via (15) based on the half-hourly averaged values. Magenta dotted lines show standard deviations for the gradient estimates of the ground flux (15).

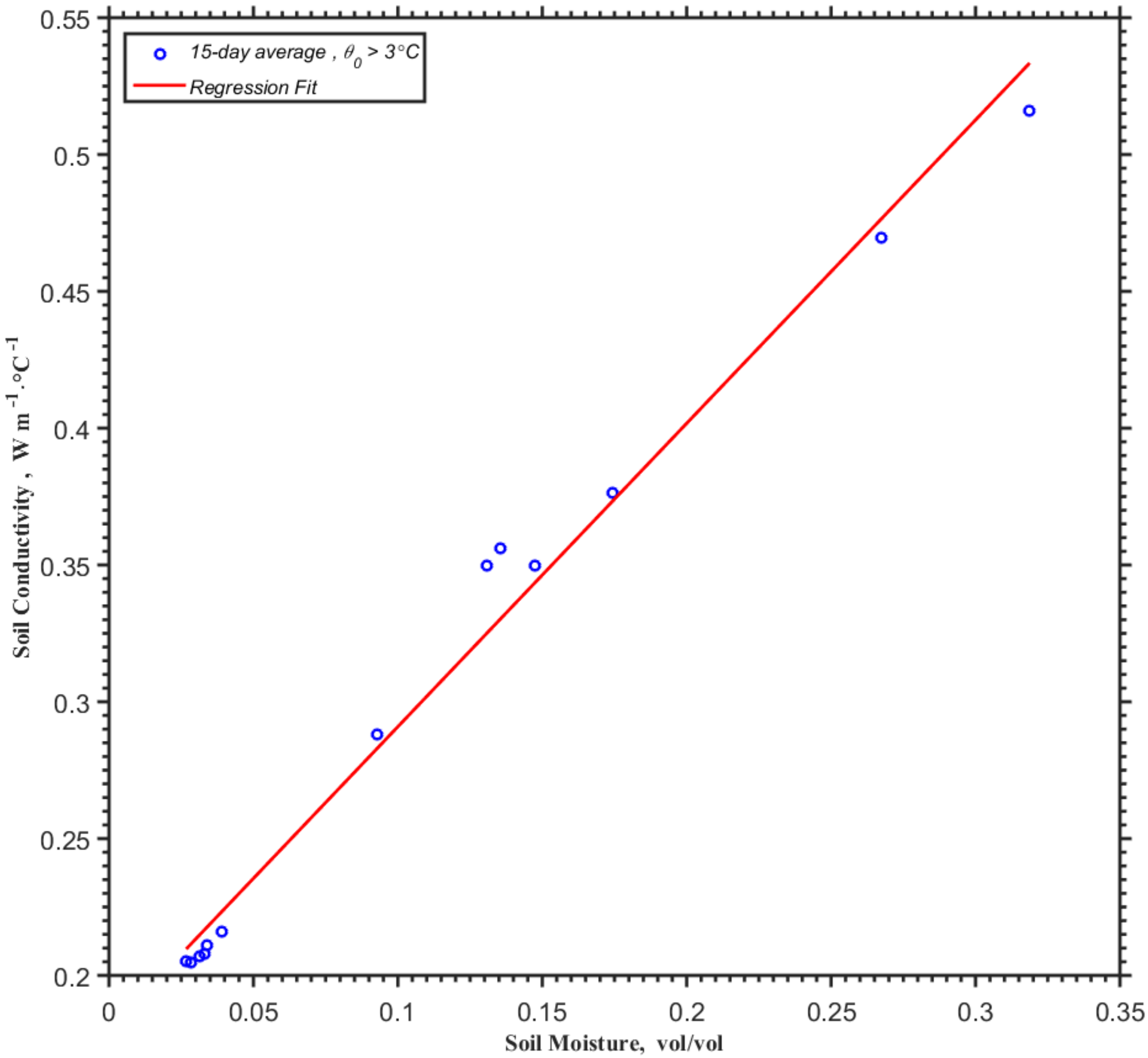

Fig. 10. Regression fit of the thermal conductivity of the soil λ versus soil moisture content at 5 cm depth Q_{S5}, see Eq. (21) based on the data collected during the entire field campaign (311-day dataset from 24 June 2016 to 01 May 2017, YD 176–487).

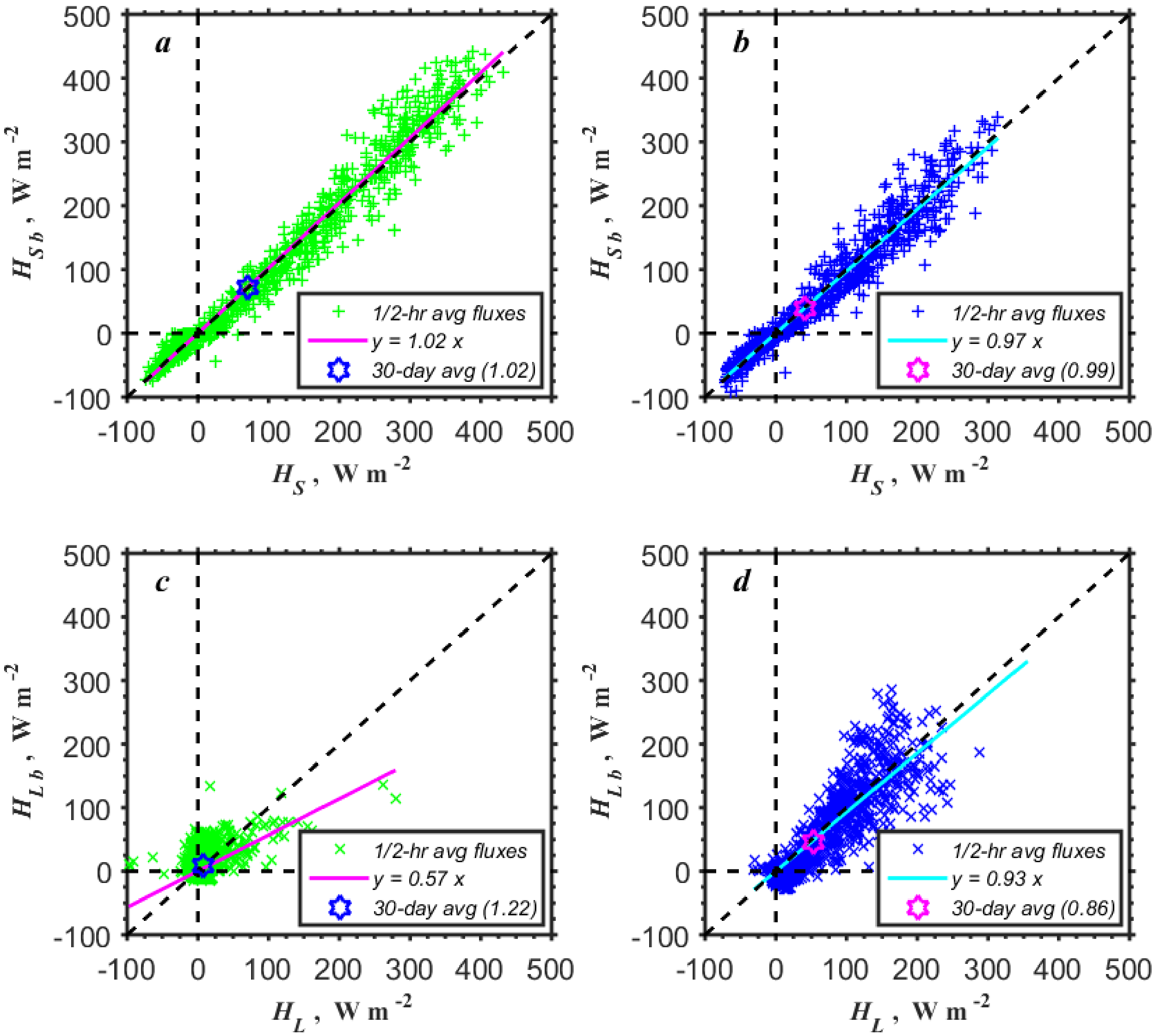

Fig. 11. Scatter plots of the bulk estimates of (a, b) sensible heat flux H_S and (c, d) latent heat flux H_L versus their measured (direct covariance) counterparts based on the half-hourly and monthly averaged data using (11) and (12) with $\alpha = 0.4 + 5Q_{S5}$ (α not to exceed 1.45). Plots in the left panels (a, c) represent the dry soil "golden files" (YD 240–270) and the right panels (b, d) represent the wet soil "golden files" period (YD 450–480). Correlation coefficients: (a) $R^2 = 0.99$, (b) $R^2 = 0.98$, (c) $R^2 = 0.56$, and (d) $R^2 = 0.88$.

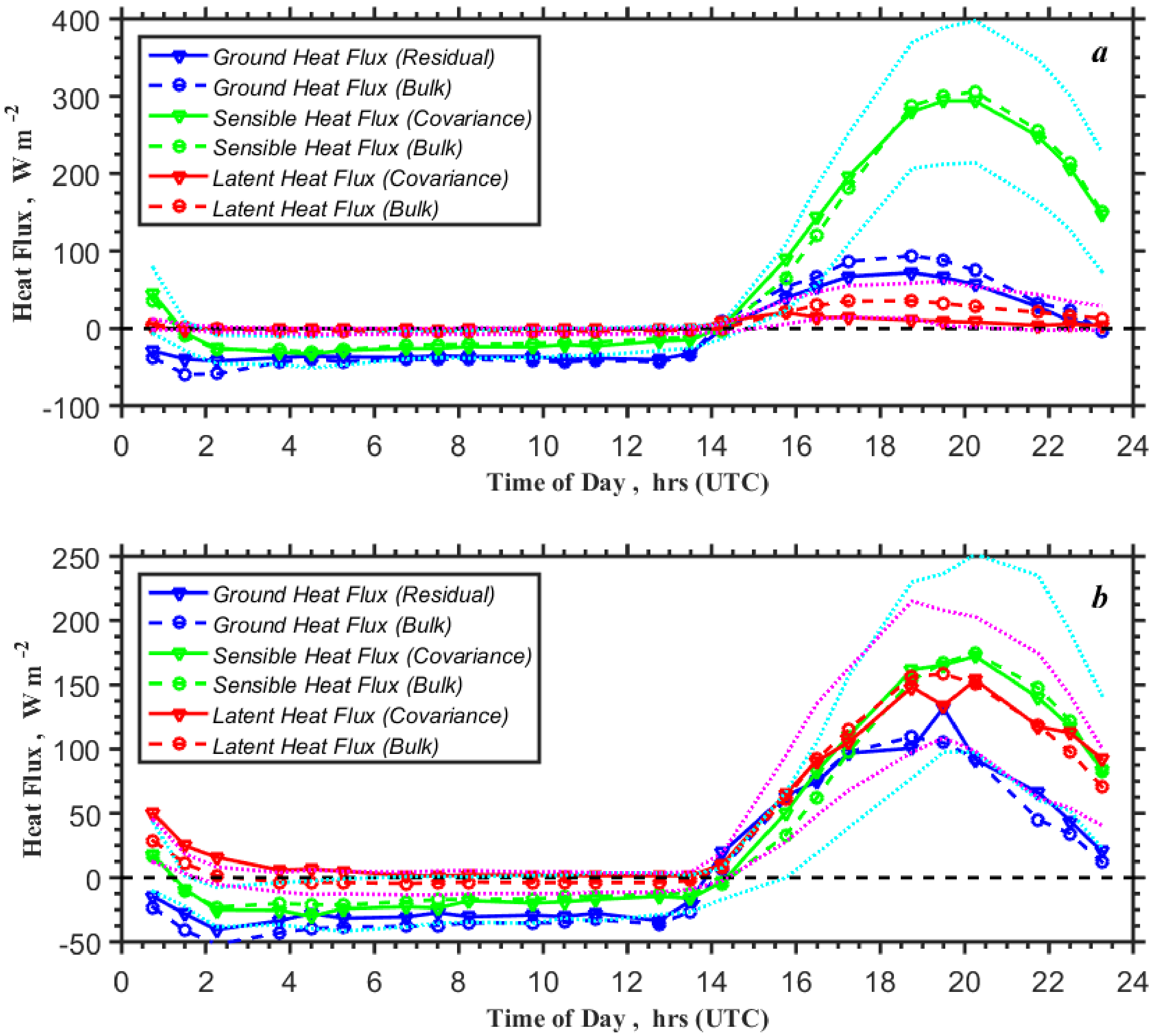

Fig. 12. Mean diurnal cycle of sensible, latent, and ground heat fluxes for (*a*) dry and (*b*) wet soil "golden files" periods. Direct measurements are solid lines with triangle symbols; the bulk estimates are dashed lines with circle symbols based on the half-hourly averaged values. Magenta and cyan dotted lines show standard deviations for the latent and sensible bulk heat fluxes respectively.

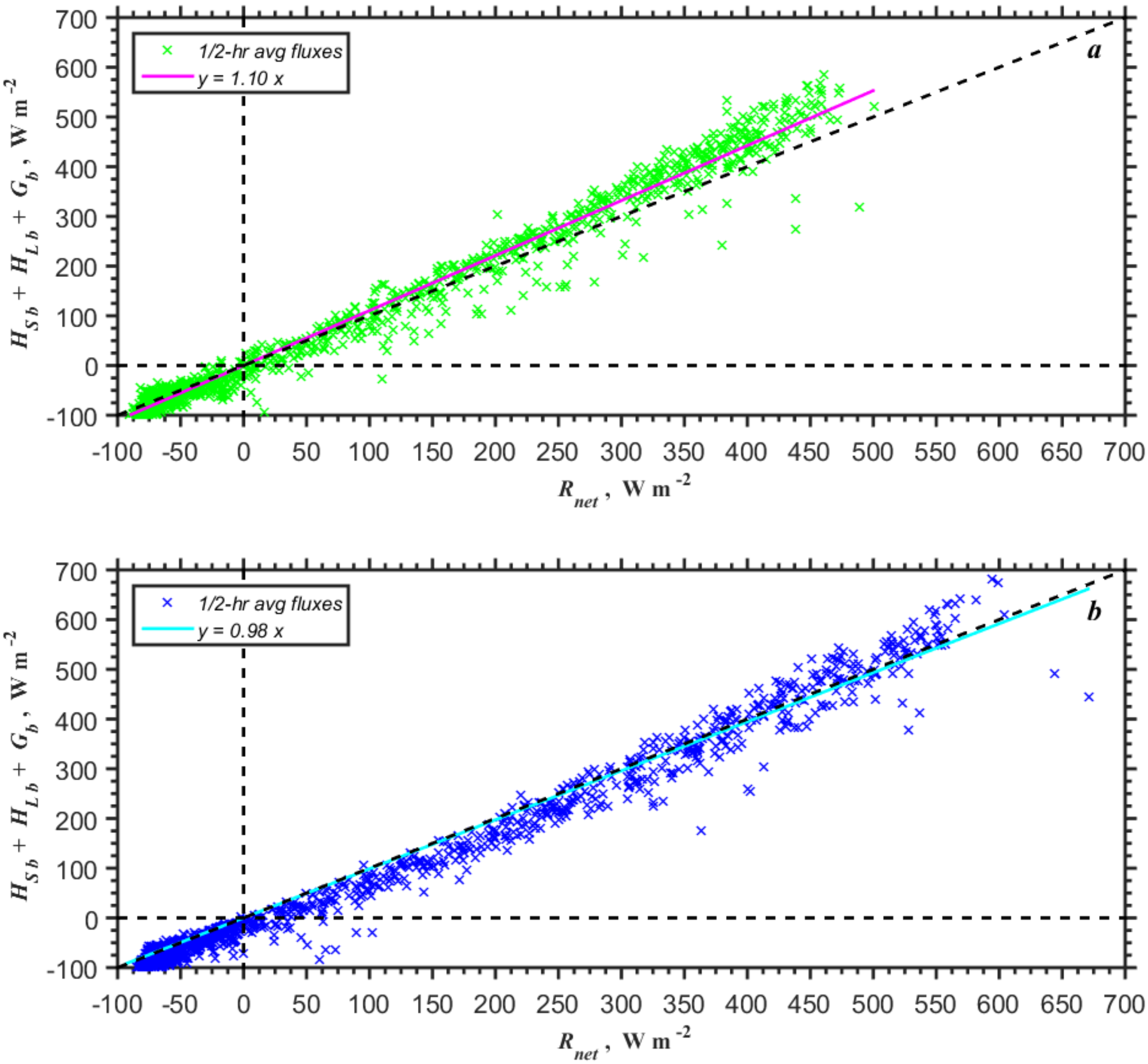

Fig. 13. Net surface energy balance from bulk flux calculations for (*a*) the dry soil "golden files" (YD 240–270) and (*b*) the wet soil "golden files" period (YD 450–480). Observed net radiation R_{net} versus the sum of the sensible, latent and ground fluxes as yielded by (9), (11), and (15). Correlation coefficients: (*a*) $R^2 = 0.99$ and (*b*) $R^2 = 0.99$.

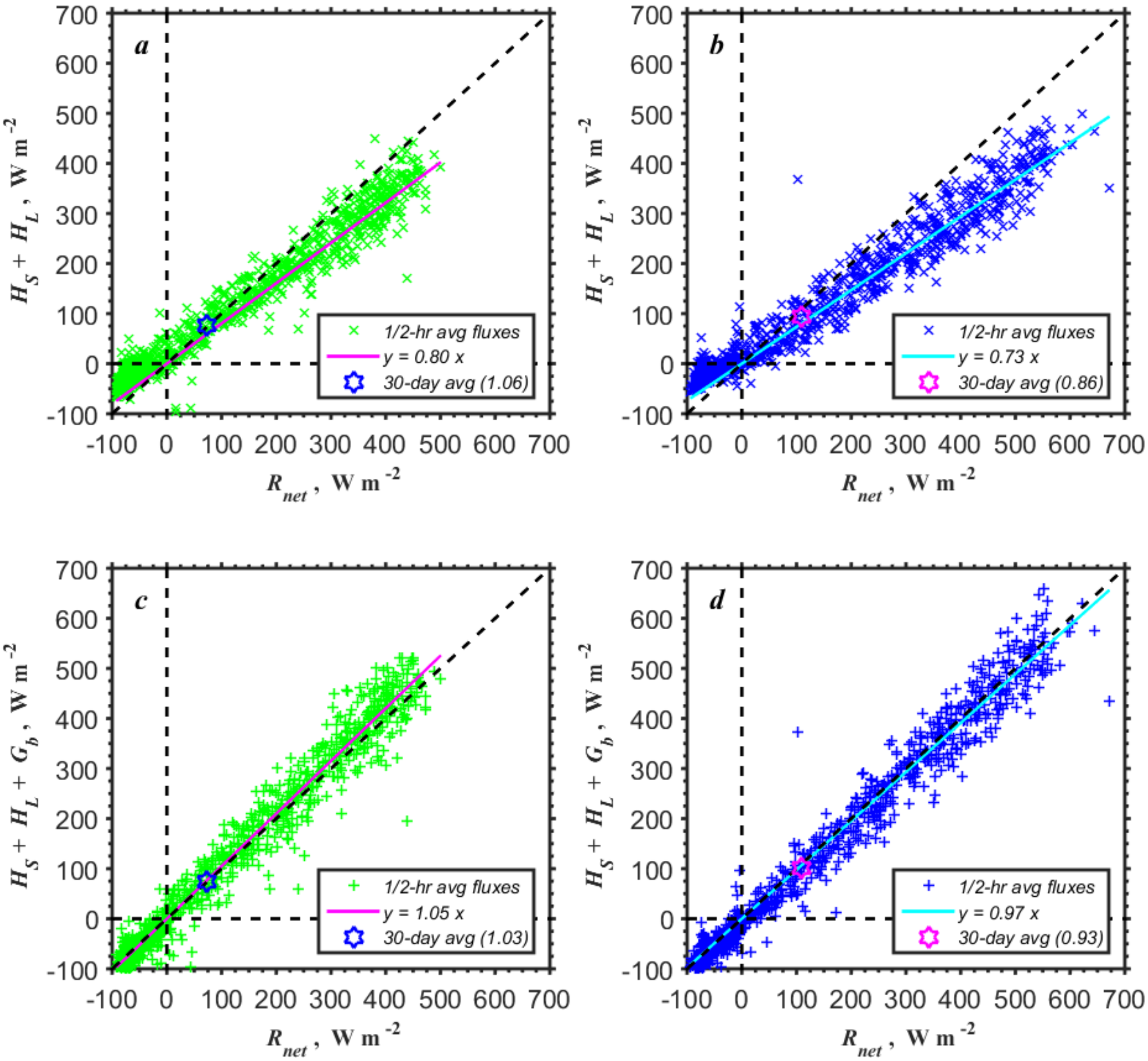

Fig. 14. Scatter plots of the net surface energy balance for (*a*, *b*) the sum of the measured sensible and latent heat fluxes $H_S + H_L$ and (*c*, *d*) the sum of the measured $H_S + H_L$ and bulk estimates of the ground heat flux G_b versus the net solar radiation R_{net} based on the half-hourly and monthly averaged data. Plots in the left panels (*a*, *c*) represent the dry soil "golden files" (YD 240–270) and the right panels (*b*, *d*) represent the wet soil "golden files" period (YD 450–480).

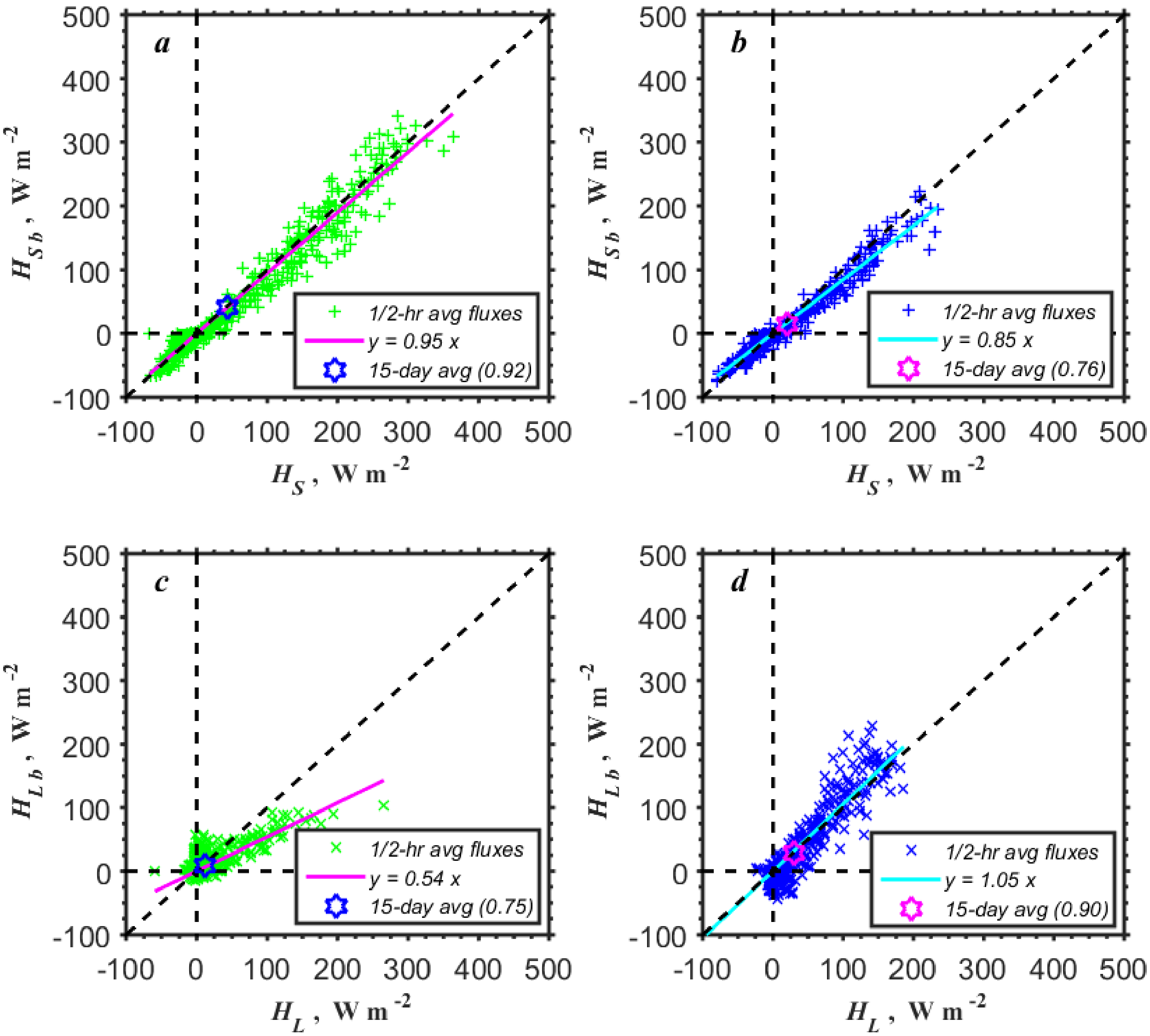

Fig. 15. Same as Fig. 11 but for (*a*, *c*) YD 270–285 (dry soils) and (*b*, *d*) YD 435–450 (wet soils). Correlation coefficients: (*a*) $R^2 = 0.98$, (*b*) $R^2 = 0.98$, (*c*) $R^2 = 0.79$, and (*d*) $R^2 = 0.92$.

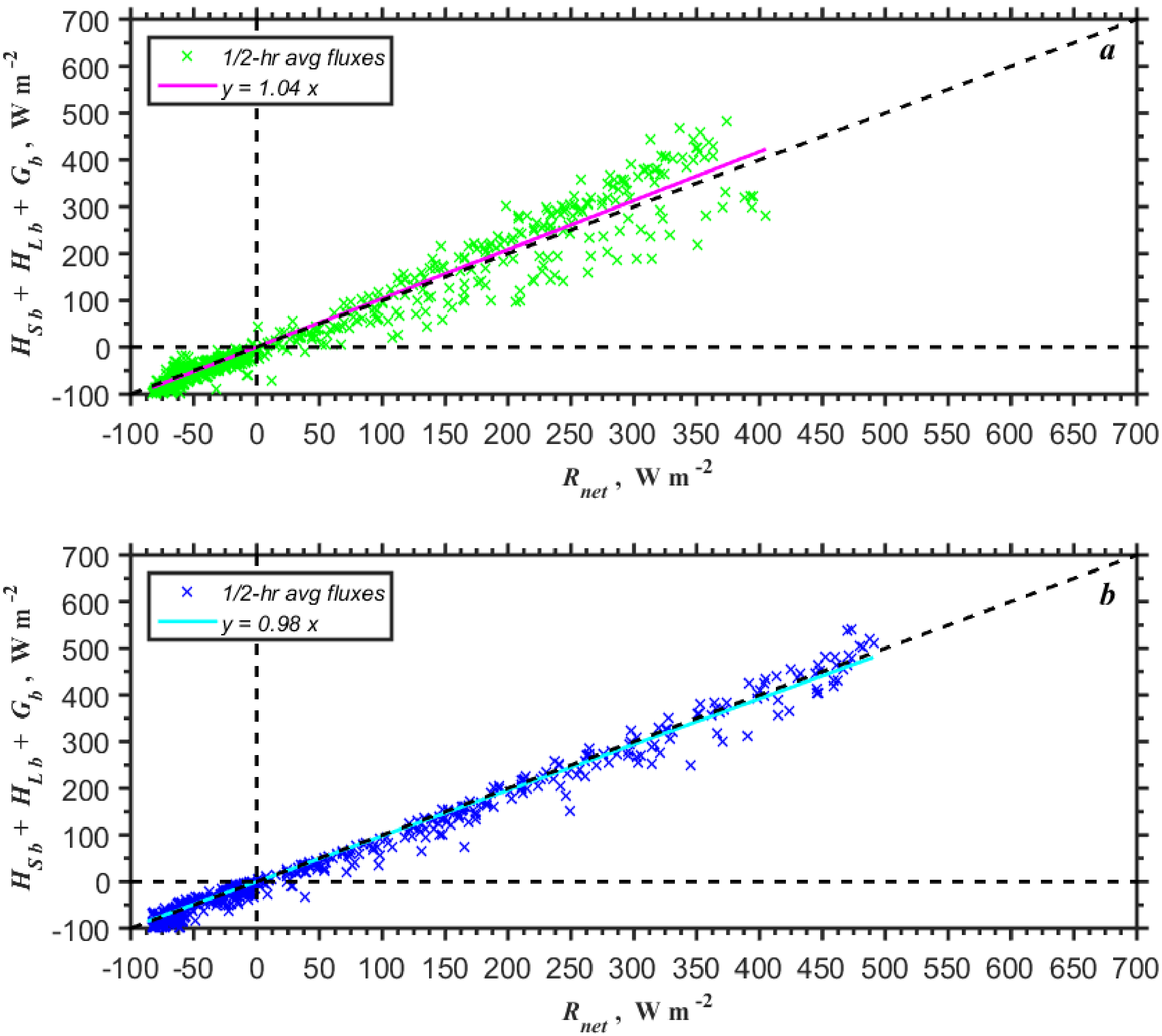

Fig. 16. Same as Fig. 13 but for (*a*) YD 270–285 (dry soils) and (*b*) YD 435–450 (wet soils). Correlation coefficients: (*a*) $R^2 = 0.97$ and (*b*) $R^2 = 0.99$.

Click here to access/download
Supplemental Material
Grachev et al SEB OR_bulk v.6_tracked changes.docx

Figure 1

Figure 2

Click here to access/download
Non-Rendered Figure
Fig 2 Grachev et al SEB OR_bulk v.6_revised.jpg

Figure 3

Click here to access/download
Non-Rendered Figure
Fig 3 Grachev et al SEB OR_bulk v.6_revised.tif

Figure 4

Figure 5

Click here to access/download
Non-Rendered Figure
Fig 5 Grachev et al SEB OR_bulk v.6_revised.tif

Figure 6

Click here to access/download
Non-Rendered Figure
Fig 6 Grachev et al SEB OR_bulk v.6_revised.tif

Figure 7

Click here to access/download
Non-Rendered Figure
Fig 7 Grachev et al SEB OR_bulk v.6_revised.tif

Figure 8

Click here to access/download
Non-Rendered Figure
Fig 8 Grachev et al SEB OR_bulk v.6_revised.png

Figure 9

Click here to access/download
Non-Rendered Figure
Fig 9 Grachev et al SEB OR_bulk v.6_revised.tif

Figure 10

Click here to access/download
Non-Rendered Figure
Fig 10 Grachev et al SEB OR_bulk v.6_revised.png

Figure 11

Click here to access/download

Non-Rendered Figure

Fig 11 Grachev et al SEB OR_bulk v6_revised.tif

Figure 12

Click here to access/download
Non-Rendered Figure
Fig 12 Grachev et al SEB OR_bulk v.6_revised.tif

Figure 13

Click here to access/download
Non-Rendered Figure
Fig 13 Grachev et al SEB OR_bulk v.6_revised.png

Figure 14

Click here to access/download
Non-Rendered Figure
Fig 14 Grachev et al SEB OR_bulk v.6_revised.png

Figure 15

Click here to access/download
Non-Rendered Figure
Fig 15 Grachev et al SEB OR_bulk v.6_revised.tif

Figure 16

Click here to access/download
Non-Rendered Figure
Fig 16 Grachev et al SEB OR_bulk v.6_revised.tif